
TOWARDS SCALABLE TOPOLOGICAL REGULARIZERS

Hiu-Tung Wong^{1,†}, Darrick Lee^{2,†}, Hong Yan¹

¹CIMDA, City University of Hong Kong, ²School of Mathematics, University of Edinburgh
 hiutung@innocimda.com, darrick.lee@ed.ac.uk, h.yan@cityu.edu.hk

ABSTRACT

Latent space matching, which consists of matching distributions of features in latent space, is a crucial component for tasks such as adversarial attacks and defenses, domain adaptation, and generative modelling. Metrics for probability measures, such as Wasserstein and maximum mean discrepancy, are commonly used to quantify the differences between such distributions. However, these are often costly to compute, or do not appropriately take the geometric and topological features of the distributions into consideration. Persistent homology is a tool from topological data analysis which quantifies the multi-scale topological structure of point clouds, and has recently been used as a topological regularizer in learning tasks. However, computation costs preclude larger scale computations, and discontinuities in the gradient lead to unstable training behavior such as in adversarial tasks. We propose the use of *principal persistence measures*, based on computing the persistent homology of a large number of small subsamples, as a topological regularizer. We provide a parallelized GPU implementation of this regularizer, and prove that gradients are continuous for smooth densities. Furthermore, we demonstrate the efficacy of this regularizer on shape matching, image generation, and semi-supervised learning tasks, opening the door towards a scalable regularizer for topological features.

1 INTRODUCTION

Latent space matching is a fundamental task in deep learning. Quantifying differences in latent representations and optimizing the network accordingly enables applications such as adversarial attack and defenses (Yu et al., 2021; Madaan et al., 2020; Lin et al., 2020), domain adaptation (Sun et al., 2016; Sun & Saenko, 2016; Long et al., 2017; Xu et al., 2019) and few-shot learning (Schonfeld et al., 2019; Xu et al., 2022; Mondal et al., 2023). Unsupervised training frameworks such as Generative Adversarial Networks (GANs) (Goodfellow et al., 2014) are fundamentally built on this concept, which is the primary framework considered throughout this article.

Topological Features of Latent Representations. The *manifold hypothesis* states that real-world high dimensional data sets are often concentrated about lower dimensional submanifolds. Recent work has empirically verified that image datasets such as CIFAR-10 and ImageNet satisfy a *union of manifolds hypothesis* (Brown et al., 2022), where the intrinsic dimension of connected components may be different. In the context of GANs, correctly learning the geometric and topological properties of these lower-dimensional structures enable meaningful interpolation in data space by traversing network latent spaces. Such properties are crucial to generalization ability (Zhou et al., 2020; Wang et al., 2021b) and generation quality (Zhu et al., 2023; Katsumata et al., 2024). Furthermore, topological metrics based on *persistent homology* provide highly effective evaluation metrics for GANs (Zhou et al., 2021; Khruikov & Oseledets, 2018; Barannikov et al., 2021; Charlier et al., 2019).

Standard approaches to latent space matching use metrics on probability measures such as the Wasserstein distance and maximum mean discrepancy (MMD) metrics, which *implicitly* take topological features into consideration. In particular, the measures (and thus all topological properties) become equivalent when the distance is trivial. However, GANs are not guaranteed to reach a global minimum, and often converge to local saddle points (Berard et al., 2019; Liang & Stokes, 2019). When measures

[†]Equal contribution.

are a finite distance apart, their topological properties may be distinct. Motivated by the above work, which demonstrates that topological similarity between real and generated distributions is a critical component of GAN performance, we propose the use of a topological regularizer which *explicitly* measures the difference between topological features at non-equilibrium states.

Persistent Homology. Persistent homology (PH) is a tool which summarizes the multi-scale topological features of a dataset in an object called a *persistence diagram*. Such topological summaries have been applied in machine learning tasks (Hensel et al., 2021), such as image segmentation (Hu et al., 2019; Clough et al., 2022; Shit et al., 2021; Waibel et al., 2022), and graph learning (Horn et al., 2021; Ballester & Rieck, 2024). The standard way to quantify the topological differences between datasets is to compute the Wasserstein distance between their persistence diagrams. However, there are two difficulties in directly applying persistence-based methods in adversarial deep learning tasks.

1. **Scalability.** Persistent homology of a large point cloud is prohibitively expensive to compute¹. Even worse, the persistent homology algorithm is highly nontrivial to parallelize. Modern PH packages are either pure CPU implementations (Bauer, 2021; Pérez et al., 2021) or use a CPU-GPU hybrid algorithm (Zhang et al., 2020).
2. **Smoothness.** Persistent homology is differentiable almost everywhere, which allows us to compute backpropagate through PH layers; in fact, stochastic subgradient descent is provably convergent with respect to persistence-based functions (Carriere et al., 2021). However, in adversarial tasks, where the loss function is constantly changing, discontinuities in the gradient leads to highly unstable training dynamics (Wiatrak et al., 2019).

Contributions. We address these two issues by modifying the two central parts of the classical persistence pipeline: the topological summary itself, as well as the metric used to compare them.

- **Topological Summary: Principal Persistence Measures.** To reduce the computational cost, we compute the persistent homology of many small batches of subsamples in parallel. By choosing a specific number of points depending on the homology dimension, the persistence computation significantly simplifies, and we obtain an object called the *principal persistence measure (PPM)* (Gómez & Mémoli, 2024). We provide a pure GPU implementation of the PPM, which enables a scalable methodology to incorporate topological features in larger-scale ML tasks. Moreover, subsampling results in a smoother features (Solomon et al., 2021), resulting in more stable training behavior.
- **Topological Metric: Maximum Mean Discrepancy for PPMs.** The Wasserstein distance is the primary metric used to compare PPMs (Gómez & Mémoli, 2024). In practice, one often uses entropic regularization to lower the computational cost (Cuturi, 2013; Lacombe et al., 2018). Despite this, it is still computationally expensive, and we use maximum mean discrepancy (MMD) metrics to compare PPMs. This coincides with the *persistence weighted kernels* introduced in (Kusano et al., 2016) for persistence diagrams. Our main theoretical results deals with establishing this metric in PPM framework.
 - Theorem 1 builds characteristic kernels for PPMs from kernels on \mathbb{R}^2 .
 - Theorem 2 shows that these MMD metrics induce the same topology as Wasserstein.
 - Theorem 3 shows that gradients with respect to this metric are continuous.

Theorem 1 and Theorem 2 adapt results from (Kusano et al., 2016; Divol & Lacombe, 2021) to the setting of PPMs, while to the authors’ knowledge, Theorem 3 is novel.

These theoretical results imply that we can use PPM-Reg as an alternative to computationally expensive Wasserstein (or Sinkhorn) metrics, which produces a stable gradient for training deeper networks. In particular, the proposed methods allow us to incorporate topological features into large-scale machine learning tasks in a stable manner (Papamarkou et al., 2024, Section 4.2). We demonstrate this empirically in Section 6, where we provide extensive experiments to demonstrate the efficacy of PPM-Reg in the GAN framework.

¹The worst-case time complexity is $O(m^3)$, where m is the number of simplices. Computing dimension k persistent homology of a point cloud with n points can have up to $m = O(n^{k+1})$ simplices. However, for practical data sets, the complexity is often much lower; see (Otter et al., 2017) for further discussion.

Related Work. The application of persistent homology in machine learning has been enabled by theoretical studies into the differentiability properties of PH (Carriere et al., 2021; Leygonie et al., 2022), which have also been extended to the multiparameter setting (Scoccola et al., 2024). However, large-scale computation of PH remains a challenge, though recent work has considered computational strategies for optimization problems (Nigmatov & Morozov, 2024; Luo & Nelson, 2024). Our MMD metric for PPMs is also related to work on kernels for persistence diagrams Kusano et al. (2016) and linear representations of persistence diagrams Divol & Lacombe (2021); Divol & Polonik (2019).

Subsampling methods for PH of metric measure spaces was introduced in (Blumberg et al., 2014), and used to approximate PH for point clouds (Chazal et al., 2015; Cao & Monod, 2022; Stolz, 2023). Furthermore, distributed approaches for computing the true PH of point clouds have been proposed in (Yoon & Ghrist, 2020; Torras-Casas, 2023) via spectral sequence methods. More recently, (Solomon et al., 2021) used subsampling methods for topological function optimization, motivated by the same issues of computational cost and instability of gradients (Bendich et al., 2020), and (Solomon et al., 2022) showed that such distributed persistence methods interpolate between geometric and topological features based on the number of subsamples. The starting point of this article is (Gómez & Mémoli, 2024), which introduces principal persistence measures.

2 LATENT SPACE MATCHING IN GENERATIVE ADVERSARIAL NETWORKS

Our primary consideration is the latent space matching in generative adversarial networks (GANs). A GAN is an unsupervised training framework consisting of a generator $g_\omega : \mathbb{R}^N \rightarrow \mathbb{R}^M$, a discriminator $d_\theta : \mathbb{R}^M \rightarrow \mathbb{R}^L$ and a value function $\mathcal{V} : \mathcal{P}(\mathbb{R}^L) \times \mathcal{P}(\mathbb{R}^L) \rightarrow \mathbb{R}$ (Goodfellow et al., 2014). Consider a set of training data, such as a collection of images, which we view as a probability measure μ on \mathbb{R}^M , the *data space*. The *generator* g_ω is parameterized by $\omega \in \mathbb{R}^G$, and its goal is to map a given noise measure ν on \mathbb{R}^N (the *noise space*) to \mathbb{R}^M such that $g_\omega(\nu)$ can be interpreted as novel examples of μ . The *discriminator* d_θ , parametrized by $\theta \in \mathbb{R}^D$, performs dimensionality reduction, sending the data space to the *latent space* \mathbb{R}^L . Finally, the *value function* is used to quantify the difference between the real data μ and the generated data $g_\omega(\nu)$ by $\mathcal{V}(d_\theta(\mu), d_\theta(g_\omega(\nu)))$.

The generator is optimized such that it minimizes the value function, while the goal of the discriminator is to maximize it. Training algorithms (Goodfellow et al., 2014; Arjovsky et al., 2017; Gulrajani et al., 2017) have been proposed to find an equilibrium of the minimax problem, given by

$$\max_{\theta} \min_{\omega} \mathcal{V}(d_\theta(\mu), d_\theta(g_\omega(\nu))). \quad (1)$$

In practice, parameters in d_θ and g_ω are updated alternatively. Common value functions used are metrics between probability distributions such as the Wasserstein distance, which has better theoretical properties in solving the minimax problem with gradient descent (Arjovsky et al., 2017), and the Cramer distance (Bellemare et al., 2017), which has unbiased gradients with mini-batch training. However, these metrics do not explicitly take topological features of the distributions into consideration. This motivates the use of a *topological regularizer*, which explicitly accounts for topological features in a non-equilibrium state. In particular, we consider value functions of the form

$$\mathcal{V} = \mathcal{L} + \lambda \mathcal{T}, \quad (2)$$

where \mathcal{L} is the main loss function, $\lambda > 0$ is a hyperparameter, \mathcal{T} is our proposed topological regularizer which will be introduced in the following sections.

3 PRINCIPAL PERSISTENCE MEASURES

We provide a streamlined exposition of the notion of principal persistence measures (Gómez & Mémoli, 2024). As there already exists several excellent references for persistent homology, we refer the reader to (Edelsbrunner & Harer, 2010; Dey & Wang, 2022; Hensel et al., 2021) for further background. Furthermore, we highlight the fact that we only consider persistent homology for simple point clouds, with an explicit definition in Equation (4). For a topological space \mathcal{X} , we use $\mathcal{P}(\mathcal{X})$ (resp. $\mathcal{P}_c(\mathcal{X})$) to denote the Borel probability measure (resp. with compact support) on \mathcal{X} . Throughout this article, we consider persistent homology of point clouds with the Vietoris-Rips filtration.

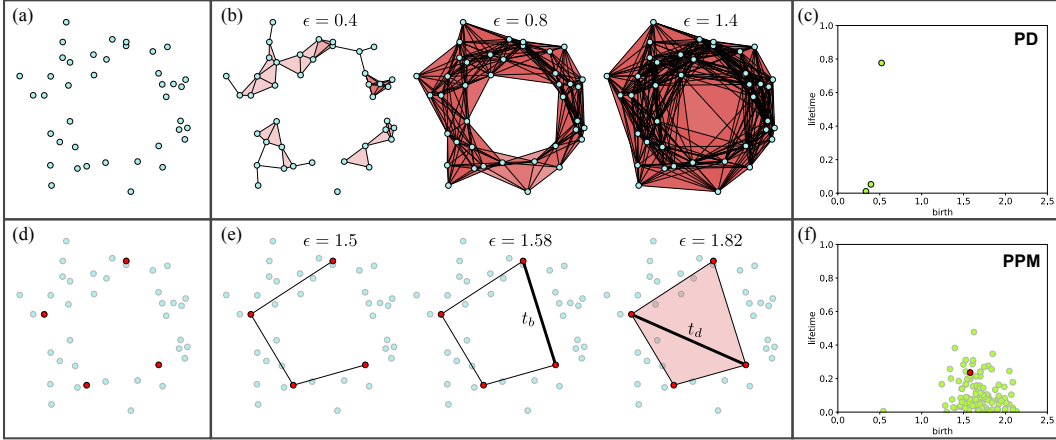


Figure 1: An illustration of PH and PPMs. (a) An example point cloud X . (b) Snapshots of the Vietoris-Rips filtration X_ϵ of X at various ϵ . Edges are added between x_i and x_j when $d(x_i, x_j) > \epsilon$ and higher simplices are added when all pairwise distances are greater than ϵ . (c) The dimension 1 persistence diagram of X in birth-lifetime coordinates. The one point with large lifetime represents the fact that there is a hole in the dataset which persists through multiple scales. (d) An example of a subsampling (in red) of $4 = 2q + 2$ points when $q = 1$. (e) Snapshots of the Vietoris-Rips filtration of the subsample, where the distances of the bold lines are t_b and t_d . (f) The dimension 1 principal persistence measure of X , where the point given by the example subsample is shown in red.

Persistent Homology. Let $X = \{x_i\}_{i=1}^N$, where $x_i \in \mathbb{R}^n$. *Persistent homology* (Edelsbrunner & Harer, 2010) of dimension $q \in \mathbb{N}$ builds a multi-scale topological summary of X in three steps:

1. Construct a sequence of topological spaces X_ϵ representing the point cloud at a scale parameter $\epsilon > 0$, equipped with inclusion maps $X_\epsilon \hookrightarrow X_{\epsilon'}$ for $\epsilon < \epsilon'$ (see Figure 1(b)).
2. Compute the *dimension q homology* of X_ϵ to obtain topological properties at each scale.
3. Track the *birth*, b , and *lifetime*, ℓ , of topological features across scales by using the induced maps $H_q(X_\epsilon) \rightarrow H_q(X_{\epsilon'})$, and summarize this information as a multi-set $\text{PH}_q(X) = \{(b_i, \ell_i)\}_{i=1}^r$ called a *persistence diagram*² (see Figure 1(c)).

The points $(b, \ell) \in \text{PH}_q(X)$ in a persistence diagram are valued in the quotient of the half plane

$$\Omega := \{(b, \ell) \in \mathbb{R}^2 : \ell \geq 0\} / \{\ell = 0\}, \quad (3)$$

as topological features $(b, \ell) \in \text{PH}_q(X)$ where points with trivial lifetime $\ell = 0$ are equivalent to the feature not existing. We view this as a pointed quotient metric space $(\Omega, d, *)$, where d is the quotient of the Euclidean metric on \mathbb{R}^2 and $*$ represents the collapsed point $\{\ell = 0\}$.

Persistent Homology of Small Point Clouds. It is shown in (Gómez & Mémoli, 2024, Theorem 4.4) that PH_q of a point cloud S with exactly $2q + 2$ points has at most a single topological feature, and can be explicitly computed as follows. Given a point $x \in S$, let $x^{(1)}, x^{(2)} \in S$ denote the points such that $d(x, x^{(1)}) \geq d(x, x^{(2)}) \geq d(x, a)$ for all $a \in S - \{x^{(1)}, x^{(2)}\}$. Then,

$$\text{PH}_q(S) = \{(t_b, t_d - t_b)\}, \quad t_b := \max_{x \in S} d(x, x^{(2)}), \quad t_d := \min_{x \in S} d(x, x^{(1)}) \quad (4)$$

whenever $t_d \geq t_b$, and $\text{PH}_q(S) = \{*\}$ otherwise (see Figure 1(e)). As we will exclusively consider PH_q of $2q + 2$ points, we will consider this as a map $\text{PH}_q : (\mathbb{R}^n)^{2q+2} \rightarrow \Omega$. We emphasize that Equation (4) is a significant simplification of the full persistent homology computation (Otter et al., 2017), and is the key to parallelized computations discussed in Section 6.1.

²Note that birth-lifetime coordinates are a linear transformation of the more standard birth-death coordinates. We use lifetime coordinates to simplify the kernel expressions in the following section.

Principal Persistence Measures. Principal persistence measures (PPMs) of dimension q (Gómez & Mémoli, 2024) contains PH_q of all subsamples S of a point cloud X with exactly $|S| = 2q + 2$ points. More formally, we will consider the more general setting of probability measures on \mathbb{R}^n with compact support rather than point clouds³ on \mathbb{R}^n . Then, the *PPM of dimension q* is defined as

$$\text{PPM}_q : \mathcal{P}_c(\mathbb{R}^n) \rightarrow \mathcal{P}(\Omega), \quad \text{PPM}_q(\mu) := (\text{PH}_q)_* \mu^{\otimes(2q+2)} \quad (5)$$

where $\mu^{\otimes n}$ is the product measure on $(\mathbb{R}^n)^{2q+2}$, and $(\text{PH}_q)_*$ is the pushforward map. In other words, we take $2q + 2$ i.i.d. samples from μ and compute PH_q on each collection to obtain a probability measure on Ω (see Figure 1(f)).

Metrics and Stability. Let $p \geq 1$, and let W_p denote the p -Wasserstein metric on \mathbb{R}^n and Ω . A key property shown in (Gómez & Mémoli, 2024, Theorem 3.8, Theorem 4.11) is that PPMs are *stable*:

$$W_p(\text{PPM}_q(\mu), \text{PPM}_q(\nu)) \leq C_q W_p(\mu, \nu), \quad \text{for all } \mu, \nu \in \mathcal{P}_c(\mathbb{R}^n) \quad (6)$$

where $C_q > 0$ is a constant which depends on q . In particular, p -Wasserstein metrics on Ω for PPMs is the analogue of the partial p -Wasserstein distance for persistence diagrams.

4 MAXIMUM MEAN DISCREPANCY FOR PPMs

In order to further reduce the computational cost and obtain smoothness properties, we will use maximum mean discrepancy (MMD) metrics to compare PPMs. The kernels defined here adapted from the *persistence weighted kernels* of Kusano et al. (2016). We assume basic familiarity with kernels and refer the reader to Appendix A for background.

Bounded PPMs and Notation. Throughout this section, we work with *bounded* PPMs valued in

$$\Omega_T := \{(b, \ell) \in [0, T]^2 : \ell \geq 0\} / \{\ell = 0\} \quad (7)$$

for some $T > 0$. We continue to denote the collapsed point by $*$. Note that for $\mu \in \mathcal{P}_c(\mathbb{R}^n)$, where the support of μ has diameter T , we have $\text{PPM}_k(\mu) \in \mathcal{P}(\Omega_T)$. In order to simplify notation, we use $\Omega = \Omega_T$ throughout this section. We use the notation $z = (b, \ell)$ for elements in both $[0, T]^2$ and Ω .

Kernels on Ω . Following the construction in Kusano et al. (2016), we introduce a procedure to turn a kernel k on $[0, T]^2$ into a kernel on Ω . Suppose $k : [0, T]^2 \times [0, T]^2 \rightarrow \mathbb{R}$ is a kernel, where \mathcal{H} is its reproducing kernel Hilbert space (RKHS), and let $\Phi : [0, T]^2 \rightarrow \mathcal{H}$ be the associated feature map given by $\Phi(z) = k(z, \cdot)$. We define a feature map $\Phi_\Omega : \Omega \rightarrow \mathcal{H}$ into the same RKHS by

$$\Phi_\Omega(z) = \ell \cdot \Phi(z) = \ell \cdot k(z, \cdot) \text{ when } \ell > 0 \quad \text{and} \quad \Phi_\Omega(*) = 0. \quad (8)$$

Then, for $z_1, z_2 \in \Omega - \{*\}$, the associated kernel $k_\Omega : \Omega \times \Omega \rightarrow \mathbb{R}$, satisfies

$$k_\Omega(z_1, z_2) := \langle \Phi_\Omega(z_1), \Phi_\Omega(z_2) \rangle_{\mathcal{H}} = \ell_1 \cdot \ell_2 \cdot k(z_1, z_2) \quad (9)$$

by the reproducing kernel property of \mathcal{H} , and $k_\Omega(*, z) = k_\Omega(z, *) = 0$. Note that k_Ω is continuous on $\Omega \times \Omega$. We denote the RKHS of k_Ω by \mathcal{H}_Ω , where we have an embedding $\mathcal{H}_\Omega \hookrightarrow \mathcal{H}$ by definition.

Characteristic Kernels on Ω . Recall that a kernel $k : \mathcal{X} \times \mathcal{X} \rightarrow \mathbb{R}$ (with associated feature map $\Phi : \mathcal{X} \rightarrow \mathcal{H}$) is *characteristic with respect to probability measures* $\mathcal{P}(\mathcal{X})$ if the *kernel mean embedding*, also denoted by $\Phi : \mathcal{P}(\mathcal{X}) \rightarrow \mathcal{H}$,

$$\Phi(\mu) := \mathbb{E}_{x \sim \mu} [\Phi(x)], \quad (10)$$

is injective. The following result shows that if we start with a characteristic kernel on $[0, T]^2$, the above procedure yields a characteristic kernel on Ω . This can be shown using similar methods as (Kusano et al., 2016, Section 3.1) in the current setting, but we provide an independent proof of a slightly stronger statement in Theorem 5 of Appendix B.

Theorem 1. *Let $k : [0, T]^2 \times [0, T]^2 \rightarrow \mathbb{R}$ be a kernel which is universal with respect to $C([0, T]^2)$ (or equivalently, characteristic with respect to $\mathcal{P}([0, T]^2)$). Then, $k_\Omega : \Omega \times \Omega \rightarrow \mathbb{R}$ is characteristic with respect to $\mathcal{P}(\Omega)$.*

³This is a special case of the metric measure spaces used in (Gómez & Mémoli, 2024). Furthermore, we can associate a point cloud $X = \{x_i\}_{i=1}^N \subset \mathbb{R}^n$, with the uniform probability measure μ_X on X .

MMD for Principal Persistence Measures. A characteristic kernel k_Ω on Ω induces a metric on $\mathcal{P}(\Omega)$ via the norm, called the *maximum mean discrepancy (MMD)*,

$$\text{MMD}_k(\nu_1, \nu_2) := \|\Phi(\nu_1) - \Phi(\nu_2)\|_{\mathcal{H}_\Omega}. \quad (11)$$

Let $\nu_1 = \frac{1}{N}(\sum_{i=1}^n \delta_{x_i} + (N-n)\delta_*)$ and $\nu_2 = \frac{1}{M}(\sum_{j=1}^m \delta_{y_j} + (M-m)\delta_*)$ be discrete measures in $\mathcal{P}(\Omega)$, with n and m nontrivial points $x_i, y_j \in \Omega - \{*\}$ respectively. The MMD is given by

$$\text{MMD}_k^2(\nu_1, \nu_2) = \frac{1}{N^2} \sum_{i,j=1}^n k_\Omega(x_i, x_j) - \frac{2}{NM} \sum_{i=1}^n \sum_{j=1}^m k_\Omega(x_i, y_j) + \frac{1}{M^2} \sum_{i,j=1}^m k_\Omega(y_i, y_j). \quad (12)$$

The normalization is with respect to the total (including $*$) numbers of points in ν_1 and ν_2 , but we only compute kernels between nontrivial points since $k_\Omega(*, z) = k_\Omega(z, *) = 0$. This enables the use of computable MMD metrics for PPMs. While the stability property in Equation (6) may no longer hold, MMD metrics yield the same topology on the space of probability measures (see also (Kusano et al., 2016, Theorem 3.2) in the finite setting). While a related result in a different context is given in (Divol & Lacombe, 2021, Proposition 5.1), we provide an independent proof in Appendix C.

Theorem 2. *Let k be a characteristic kernel on Ω . The p -Wasserstein metric W_p and the MMD metric MMD_k induce the same topology on $\mathcal{P}(\Omega)$.*

Remark 1. *By viewing persistence diagrams as measures (Divol & Lacombe, 2021; Giusti & Lee, 2023; Bubenik & Elchesen, 2022), persistence diagrams can be viewed as elements in $\mathcal{M}_{\text{lin}}(\Omega)$, defined in Equation (30). This includes persistence diagrams with possibly infinite cardinality (with finite total persistence). While in Kusano et al. (2016), analogous kernels are defined for finite persistence diagrams, our results hold for persistence measures in $\mathcal{M}_{\text{lin}}(\Omega)$.*

5 TOPOLOGICAL REGULARIZATION WITH PPMs

In this section, we introduce our proposed topological regularizer based on computing the PPM of probability measures and comparing the PPMs using MMD. Let k_Ω be a characteristic kernel as defined in the previous section. Returning to the notation of Section 2, we define our dimension q topological regularizer, PPM-Reg, on the latent space \mathbb{R}^L by $\mathcal{T}_q : \mathcal{P}_c(\mathbb{R}^L) \times \mathcal{P}_c(\mathbb{R}^L) \rightarrow \mathbb{R}$ by

$$\mathcal{T}_q(\mu, \nu) := \text{MMD}_{k_\Omega}(\text{PPM}_q(\mu), \text{PPM}_q(\nu)) = \|\Phi_\Omega(\text{PPM}_q(\mu)) - \Phi_\Omega(\text{PPM}_q(\nu))\|_{\mathcal{H}_\Omega}. \quad (13)$$

When we apply this in the GAN setting, we consider $\mathcal{T}_q(d_\theta(\mu), d_\theta(g_\omega(\nu)))$, where $\nu \in \mathcal{P}_c(\mathbb{R}^N)$ is the noise measure, and $\mu \in \mathcal{P}_c(\mathbb{R}^M)$ is the data measure. Let $\mathfrak{T}_q : \mathbb{R}^G \times \mathbb{R}^D \rightarrow \mathbb{R}$ be

$$\mathfrak{T}_q(\omega, \theta) := \mathcal{T}_q(d_\theta(\mu), d_\theta(g_\omega(\nu))). \quad (14)$$

Our main result of this section is to show that \mathfrak{T}_q is smooth with respect to ω and θ given sufficient smoothness conditions on the underlying measures and the discriminator and generator. Recall that a function $f : \mathbb{R}^n \rightarrow \mathbb{R}^m$ is a C^1 function if all first derivatives of f are continuous. The following is our main theoretical result, proved in Appendix D.

Theorem 3. *Let k_Ω be a characteristic kernel. Suppose $\mu \in \mathcal{P}_c(\mathbb{R}^M)$ and $\nu \in \mathcal{P}_c(\mathbb{R}^N)$ have C^1 densities. Suppose the joint functions $G : \mathbb{R}^G \times \mathbb{R}^N \rightarrow \mathbb{R}^M$ defined by $G(\omega, x) = g_\omega(x)$ and $D : \mathbb{R}^D \times \mathbb{R}^M \rightarrow \mathbb{R}^L$ defined by $D(\theta, y) = d_\theta(y)$ be C^1 functions. Then, \mathfrak{T}_q is a C^1 function wherever the PPM is not the trivial measure at the origin.*

6 EXPERIMENTS AND RESULTS

We provide empirical experiments which demonstrates the efficacy of PPM-Reg as a topological regularizer. First, in Section 6.2, we provide an expository shape matching experiment to illustrate the behavior of PPM-Reg, and provide computational comparisons. Next, in Section 6.3, we apply PPM-Reg to a GAN-based generative modelling problem, consistently improving the *generative* quality of GANs. Finally, in Section 6.4, we consider a GAN-based semi-supervised learning problem, which demonstrates the effectiveness of PPM-Reg in improving the *discriminative* ability of GANs. Due to space limitations, we have placed implementation details and additional experiments for each of the three settings in Appendix E, Appendix F, and Appendix G.⁴

⁴Code and supplementary material: <https://openreview.net/forum?id=FjZcwQJX8D>.

6.1 COMPUTATIONAL SETUP AND IMPLEMENTATION OVERVIEW

Cramer Distance. The Wasserstein and Cramer distance are both probability metrics that are sensitive to the geometry of the change in distribution (Bellemare et al., 2017). Moreover, the Cramer distance does not depend on hyperparameters which simplifies our comparison. We primarily use the Cramer metric as our main loss function \mathcal{L} . Following the definition of (Bellemare et al., 2017), for $\mu, \nu \in \mathcal{P}(\mathbb{R}^d)$. The Cramer Distance $\mathcal{E}(\mu, \nu)$ is defined as

$$\mathcal{E}(\mu, \nu) := \mathbb{E}_{x \sim \mu} [\mathcal{D}(x)] - \mathbb{E}_{y \sim \nu} [\mathcal{D}(y)], \quad \mathcal{D}(z) := \mathbb{E}_{y' \sim \nu} [\|z - y'\|_2] - \mathbb{E}_{x' \sim \mu} [\|z - x'\|_2]$$

where x, x' (resp. y, y') are independent random variables with law μ (resp. ν). We do not take the gradient estimation in (Bellemare et al., 2017, Appendix C.3) as we obtain sufficient samples.

Implementation of PPM. For all experiments, we use s subsamples from $\mu^{\otimes(2q+2)}$ to approximate the PPM (using the same number of subsamples for dimension 0 and 1). The persistent homology of each subsample is computed using Equation (4) in parallel on the GPU. Throughout these experiments, our base kernel is the radial basis function (RBF) kernel $k_{\text{RBF}}(z_1, z_2) = \exp(-\|z_1 - z_2\|^2/2\sigma)$, where the width $\sigma > 0$ is a hyperparameter. Thus, the induced kernel $k_{\Omega} : \Omega \times \Omega \rightarrow \mathbb{R}$ from Equation (9) evaluated on $z_i = (b_i, \ell_i) \in \Omega$ is

$$k_{\Omega}(z_1, z_2) = \ell_1 \cdot \ell_2 \exp(-\|z_1 - z_2\|^2/2\sigma). \quad (15)$$

We use Equation (12) to compute the MMD metric between PPMs. Furthermore, we use a weighted combination of dimension 0 and 1 PPM in our topological regularizer, such that

$$\mathcal{T} = \lambda_0 \mathcal{T}_0 + \lambda_1 \mathcal{T}_1, \quad (16)$$

where the *weights* $\lambda_0, \lambda_1 > 0$ are hyperparameters. We will call this **PPM-Reg**.

6.2 SHAPE MATCHING

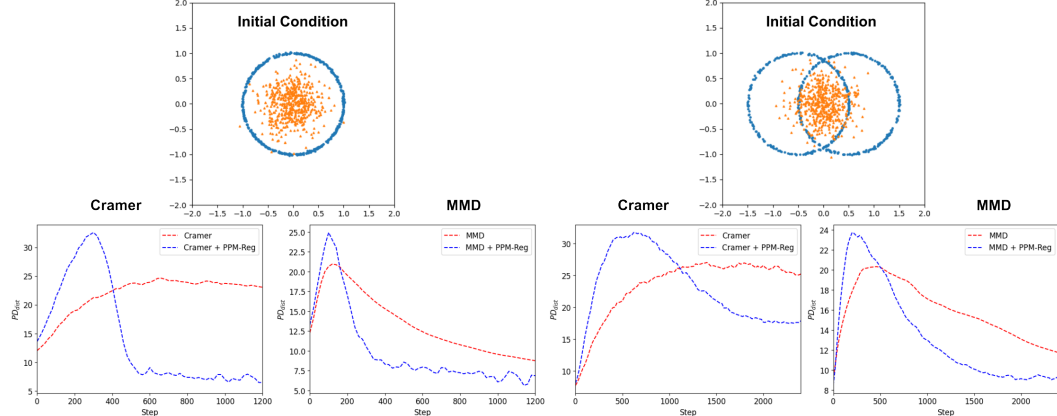


Figure 2: Visual example of PPM-Reg in a shape matching experiment using Cramer or MMD as the main loss function. 1st row: Plots of a reference point cloud (in blue) and the initial condition of a random point cloud (in orange). 2nd Row: Plots of 2-Wasserstein distance between 1-dimensional persistent homology between the reference shape and training shape over optimization steps.

Our task is to optimize the individual points of a point cloud to match the “shape” of a reference point cloud using a loss function of the form $\mathcal{L} + \mathcal{T}$, which operates directly on the ambient space of the point clouds. We choose \mathcal{L} to either be the Cramer distance (Bellemare et al., 2017) or an MMD metric using an RBF kernel (with width $\sigma = 0.1$). Our aim in this expository experiment is twofold.

1. Demonstrate the ability of PPM-Reg to regularize *topological* features in point clouds by comparing the true (non-subsampled) persistence diagrams of the trained and reference shapes. Our focus is on showing that this occurs near the beginning of the optimization, since in GAN settings, the regularization is important away from global minima (see Introduction).
2. Show the computational efficiency of PPM-Reg, which enables its use in later experiments.

Shape Matching Experiment. Our main results are summarized in Figure 2. We choose two reference shapes in \mathbb{R}^2 for visualization purposes: a circle, and the union of two intersecting circles. In the second row of Figure 2, we plot the 2-Wasserstein distance between the 1-dimensional full (non-subsampled) persistence diagrams between the fixed reference and the trained point cloud, as a function of optimization steps. In each case, we see that adding PPM-Reg significantly reduces the topological distance. An interesting feature of each of these plots is that there is an initial spike in the PD distance when using PPM-Reg. Empirically, this is due to the fact that the point cloud must first move through a regime with trivial topological structure before PPM-Reg can faithfully match the topology of the reference. The training behavior is best understood by observing the dynamics of the optimization, and we provide animations of these experiments in the supplementary material.

Computational Comparisons. The efficiency of the PPM-Reg is derived from two major components: the parallelizable PPM and the iterative-free MMD. Table 1 empirically shows the computational benefit of each component as the size of the point cloud and the number of subsamples s are varied. We use Cramer as the main loss, and consider the computational cost of using PPM-Reg, W-PPM-Reg and PD-Reg. **PD-Reg** computes the 2-Wasserstein distance between dimension 0 and 1 full persistent homology with Vietoris-Rips filtration. **W-PPM-Reg** computes the 2-Wasserstein distance between PPMs of dimension 0 and 1. We use the `torch-topological` package (Lab) to compute persistent homology and Wasserstein distances.

Our aim is to compare the real-world usage of these methods using the circle experiment. Thus, PPM-Reg computations are performed on a GPU, while PD-Reg and W-PPM-Reg uses hybrid CPU-GPU methods. The computational cost of PD-Reg grows exponentially with respect to the size of the point cloud. While the computational cost of W-PPM-Reg is sublinear with respect to the size of the point cloud, the cost is exponential with respect to the number of subsamples s . Remarkably, due to parallelization, PPM-Reg is sublinear with respect to the number of subsamples s and is nearly constant as the size of the point cloud increases. In the following experiments, we find that $s = 1024$ and $s = 2048$ performs well in practice. In summary, using MMD mediates the drawback of the increased number of features extracted by PPM, resulting in our significantly faster PPM-Reg. With parallelization, our pure PyTorch implementation of PPM-Reg outperforms highly optimized low-level CPU implementations used in `torch-topological`.

| No. points | Cramer + PPM-Reg | | | Cramer + W-PPM-Reg | | | Cramer + PD-Reg |
|------------|------------------|--------------|--------------|--------------------|---------------|----------------|-----------------|
| | s = 512 | s = 1024 | s = 2048 | s = 512 | s = 1024 | s = 2048 | |
| 128 | 0.55 ± 0.005 | 0.61 ± 0.007 | 0.98 ± 0.004 | 3.06 ± 0.033 | 13.28 ± 0.198 | 73.00 ± 3.323 | 1.99 ± 0.048 |
| 256 | 0.56 ± 0.008 | 0.61 ± 0.005 | 0.99 ± 0.005 | 3.25 ± 0.083 | 14.04 ± 0.187 | 80.11 ± 2.545 | 10.43 ± 0.075 |
| 512 | 0.56 ± 0.010 | 0.61 ± 0.014 | 0.98 ± 0.006 | 3.43 ± 0.111 | 16.43 ± 0.458 | 91.29 ± 3.081 | 107.11 ± 2.837 |
| 1024 | 0.57 ± 0.005 | 0.61 ± 0.005 | 1.00 ± 0.007 | 3.90 ± 0.092 | 19.45 ± 0.468 | 121.76 ± 3.424 | 655.58 ± 11.823 |

Table 1: Running time of 100 gradient steps (in seconds) in matching circle form randomly initialize gaussian in \mathbb{R}^2 with GPU computation enable. The averages are computed over 10 runs.

Imperfect Convergence. In Appendix E.2, we observe the same trends in additional modified experiments, which prevent the centroid of the trained shape from converging to the centroid of the reference. This is done to mimic the GAN setting where training algorithms often converge to saddle points rather than global minima (Berard et al., 2019; Liang & Stokes, 2019).

6.3 UNCONDITIONAL IMAGE GENERATION

Next, we consider the use of PPM-Reg in an unconditional image generation task, which is the standard benchmark to evaluate GANs (Goodfellow et al., 2014; Arjovsky et al., 2017).

Network Architecture and Implementation Details. We use a ResNet based CNN as the generator g_ω , which takes a 128-dimensional noise vector as input. We use a CNN as the discriminator d_θ and the output of the network is a 128-dimensional latent vector. We compare the Cramer value function $\mathcal{V} = \mathcal{L}$, with the use of PPM-Reg $\mathcal{V} = \mathcal{L} + \mathcal{T}$. As our network differs from (Bellemare et al., 2017), we retrain both regularized and unregularized networks for a fair comparison.

Dataset and Evaluation Metrics. We consider the CelebA (Liu et al., 2015) and AnimeFace (Churchill & Chao, 2019) datasets. Images are centered and resized to 32×32 . While the Fréchet Inception Distance (FID) (Heusel et al., 2017) is a popular metric to evaluate the distance between generated and real images, recent empirical work has thoroughly investigated several drawbacks of FID (Horak et al., 2021; Stein et al., 2024; Jayasumana et al., 2024). Instead, we adopt three metrics:

1. CMMD (Jayasumana et al., 2024): MMD of CLIP embeddings (Radford et al., 2021),
2. FD_{Dinov2} (Stein et al., 2024): Fréchet Distance of Dinov2 (Oquab et al., 2024) embeddings
3. WD_{latent} : 2-Wasserstein distance of CLIP embeddings (Radford et al., 2021)

In Table 2, these are computed by sampling / generating 10K images from the data set / network. We report CMMD, FD_{Dinov2} and WD_{latent} using the epoch with the smallest CMMD.

| | AnimeFace | | | CelebA | | |
|---------------------------------|-----------|---------------|---------------|--------|---------------|---------------|
| | CMMD | FD_{Dinov2} | WD_{latent} | CMMD | FD_{Dinov2} | WD_{latent} |
| Cramer (Bellemare et al., 2017) | 0.73 | 953.99 | 0.6294 | 0.72 | 722.86 | 0.6795 |
| Cramer + PPM-Reg | 0.56 | 780.68 | 0.6080 | 0.58 | 700.73 | 0.6666 |

Table 2: Quantitative evaluation on 32×32 image generation, values are reported at the epoch with the smallest CMMD.

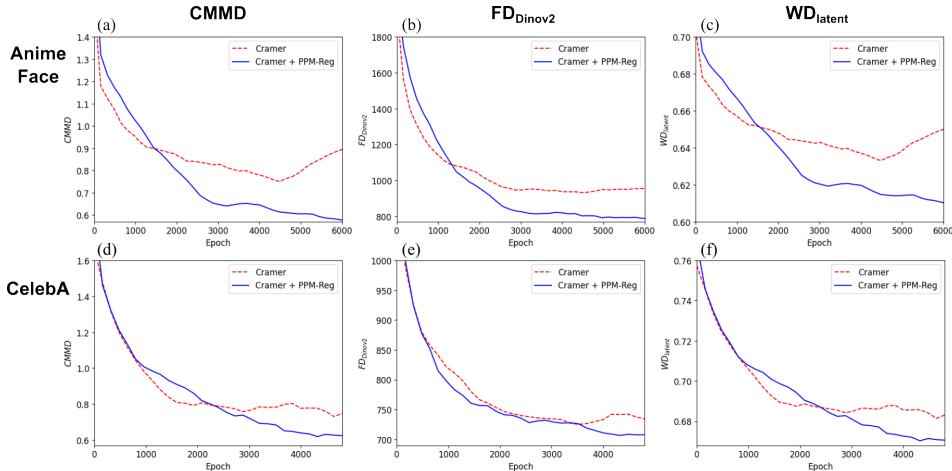


Figure 3: CMMD (a,d), FD_{Dinov2} (b,e) and WD_{latent} (c,f) versus training epochs for the AnimeFace (a-c) and CelebA (d-f) dataset. 10K samples are randomly generated to compute distances; moving averages with a window of 5 are used to smooth the values. Distances recorded every 160 epochs.

Results. Figure 3 tracks these three metrics during training. Figure 3 (a,b,d,e) shows that using PPM-Reg improves image generation quality for both AnimeFace and CelebA. The Wasserstein distance can better detect geometric information in embedding space. Tracking WD_{latent} in Figure 3 (c,f) shows that adding PPM-Reg provides more information and helps discover geometric structures in the latent space in an unsupervised way. This reinforces work that shows that persistence-based methods are able to effectively measure image generation quality (Zhou et al., 2021; Khrukov & Oseledets, 2018; Barannikov et al., 2021; Charlier et al., 2019). As training progresses, improved Cramer loss does not always lead to improved evaluation metrics (Figure 3 (a,c)). Our reported results use CMMD as an early stopping criterion which is prohibitively expensive to compute in practice. In contrast, the evaluation metrics consistently decrease with respect to training time, and this implies that may not need to compute additional metrics for early stopping. In Appendix F.2, we consider larger (64×64) image generation experiments with the CelebA and LSUN Kitchen datasets, and find similarly improved results, demonstrating the efficacy of PPM-Reg in larger-scale experiments.

6.4 SEMI-SUPERVISED LEARNING

Semi-supervised learning (SSL) methods use unlabeled data alongside a small amount of labeled data to train a classification network (Yang et al., 2022). SSL often assumes that classification problems are supported on low-dimensional manifolds, which allows a network to learn the classification problem with limited labels (Niyogi, 2013). In practice, knowledge of the low-dimensional manifold can be learned by encoding the unlabeled data to latent representations. With few labeled data points, a simple classifier is trained using those latent representations (Wang et al., 2021a; Decourt & Duong, 2020; Truong et al., 2019; Das et al., 2021). Here, we demonstrate PPM-Reg can help encode more informative latent representations, and significantly reduce classification error in SSL.

Network Architecture and Implementation Details. We use a deconvolutional network as g_ω , which takes a 64 dimension noise vector as input. We use a CNN as d_θ and the output of the network is a 64 dimension latent vector. We use an MLP as a classifier parameterized by γ , termed c_γ . We first learn the latent representations using a Cramer GAN (Bellemare et al., 2017) framework with all available data, and compare it against the addition of PPM-Reg. After training the GAN, the discriminator d_θ is frozen and its output is used as the features to train the classifier c_γ with the subset of training samples. For a comparison without latent representations learning, we consider a “Baseline”, where d_θ and c_γ are trained together as a classifier (without the generative part).

Dataset and Evaluation Metrics. We compare the SSL performance with Fashion-MNIST (Xiao, 2017), Kuzushiji-MNIST (Clanuwat et al., 2018) and MNIST. In these experiments, 200 and 400 labels are randomly sampled from the data set. Due to the inherent randomness in sampling few labels, experiments are repeated ten times and the statistics of the best test-set accuracy are reported.

| Number of labels | Fashion-MNIST | | Kuzushiji-MNIST | | MNIST | |
|------------------|---------------------|---------------------|---------------------|---------------------|---------------------|---------------------|
| | 200 | 400 | 200 | 400 | 200 | 400 |
| Baseline | 67.18 ± 0.95 | 71.00 ± 0.83 | 48.40 ± 1.79 | 55.10 ± 1.55 | 80.52 ± 1.49 | 86.39 ± 1.14 |
| Cramer | 62.70 ± 1.25 | 68.58 ± 1.08 | 47.77 ± 1.40 | 56.06 ± 1.88 | 71.10 ± 1.52 | 78.26 ± 1.30 |
| Cramer + PPM-Reg | 76.84 ± 1.23 | 80.59 ± 0.69 | 75.78 ± 1.99 | 79.33 ± 1.69 | 96.62 ± 0.39 | 97.33 ± 0.21 |

Table 3: Test-set classification accuracy (%) on Fashion-MNIST, Kuzushiji-MNIST and MNIST. with 200 and 400 labeled examples. The average and the error bar are computed over 10 runs.

Result. Table 3 shows the test classification accuracy, where we use only 0.33% (200) and 0.66% (400) of the total number of labels. Compared with Baseline, only using Cramer does not significantly improve the classification accuracy in SSL. Note that while the Cramer GAN (without PPM-Reg) has reasonable generative ability, shown in Figure 7, this does not imply strong discriminator performance in SSL. Remarkably, using PPM-Reg significantly improves the classification accuracy. For example, compared with the Baseline, Kuzushiji-MNIST has gain 27.38% improvement with 200 labels. Notably, with the latent representations learned with PPM-Reg, we can get a good accuracy using only 0.66% of the labels. This section demonstrates that discovering topological structures in latent space is not only useful in generative tasks, but can be leveraged to massively improve classification accuracy when very few labels are available. In Appendix G.2, we observe similar performance gains in additional experiments on the SVHN dataset.

7 CONCLUSION

In this article, we propose a novel method for stable and scalable topological regularization based on the subsampling principle of PPMs, opening up the possibility of detecting topological information in larger-scale machine learning problems. We introduced a theoretical framework for using kernel methods and MMD metrics for PPMs, and demonstrated the efficacy of this methodology in a variety of experimental settings. This work suggests several directions for future study. From the theoretical and computational perspective, can we develop parallelizable approximate computations in more general settings? From an applied perspective, how can we leverage approximate topological summaries in further machine learning tasks such as classification or regression?

ACKNOWLEDGMENTS

This work was supported by the Hong Kong Innovation and Technology Commission (InnoHK Project CIMDA).

REFERENCES

- Martin Arjovsky, Soumith Chintala, and Léon Bottou. Wasserstein generative adversarial networks. In *International conference on machine learning*, pp. 214–223. PMLR, 2017.
- N. Aronszajn. Theory of reproducing kernels. *Trans. Amer. Math. Soc.*, 68(3):337–404, 1950. ISSN 0002-9947. doi: 10.2307/1990404.
- Rubén Ballester and Bastian Rieck. On the Expressivity of Persistent Homology in Graph Learning, June 2024.
- Serguei Barannikov, Ilya Trofimov, Grigorii Sotnikov, Ekaterina Trimbach, Alexander Korotin, Alexander Filippov, and Evgeny Burnaev. Manifold topology divergence: A framework for comparing data manifolds. In A. Beygelzimer, Y. Dauphin, P. Liang, and J. Wortman Vaughan (eds.), *Advances in Neural Information Processing Systems*, 2021.
- Ulrich Bauer. Ripser: Efficient computation of Vietoris–Rips persistence barcodes. *Journal of Applied and Computational Topology*, 5(3):391–423, September 2021. ISSN 2367-1734. doi: 10.1007/s41468-021-00071-5.
- Marc G Bellemare, Ivo Danihelka, Will Dabney, Shakir Mohamed, Balaji Lakshminarayanan, Stephan Hoyer, and Rémi Munos. The cramer distance as a solution to biased wasserstein gradients. *arXiv preprint arXiv:1705.10743*, 2017.
- Paul Bendich, Peter Bubenik, and Alexander Wagner. Stabilizing the unstable output of persistent homology computations. *Journal of Applied and Computational Topology*, 4(2):309–338, June 2020. ISSN 2367-1734. doi: 10.1007/s41468-019-00044-9.
- Hugo Berard, Gauthier Gidel, Amjad Almahairi, Pascal Vincent, and Simon Lacoste-Julien. A closer look at the optimization landscapes of generative adversarial networks. In *International Conference on Learning Representations*, 2019.
- Andrew J. Blumberg, Itamar Gal, Michael A. Mandell, and Matthew Pancia. Robust Statistics, Hypothesis Testing, and Confidence Intervals for Persistent Homology on Metric Measure Spaces. *Found. Comput. Math*, 14(4):745–789, August 2014. ISSN 1615-3383. doi: 10.1007/s10208-014-9201-4.
- Bradley CA Brown, Anthony L Caterini, Brendan Leigh Ross, Jesse C Cresswell, and Gabriel Loaiza-Ganem. Verifying the union of manifolds hypothesis for image data. *arXiv preprint arXiv:2207.02862*, 2022.
- Peter Bubenik and Alex Elchesen. Virtual persistence diagrams, signed measures, Wasserstein distances, and Banach spaces. *Journal of Applied and Computational Topology*, 6(4):429–474, December 2022. ISSN 2367-1734. doi: 10.1007/s41468-022-00091-9.
- Yueqi Cao and Anthea Monod. Approximating Persistent Homology for Large Datasets, May 2022.
- Mathieu Carriere, Frederic Chazal, Marc Glisse, Yuichi Ike, Hariprasad Kannan, and Yuhei Umeda. Optimizing persistent homology based functions. In *Proceedings of the 38th International Conference on Machine Learning*, pp. 1294–1303. PMLR, July 2021.
- Jeremy Charlier, Radu State, et al. PHom-GeM: Persistent homology for generative models. In *The 6th Swiss Conference on Data Science (SDS), 2019 IEEE International Conference*. IEEE, 2019.
- Frédéric Chazal, Brittany Terese Fasy, Fabrizio Lecci, Bertrand Michel, Alessandro Rinaldo, and Larry Wasserman. Subsampling methods for persistent homology. In *Proceedings of the 32nd International Conference on International Conference on Machine Learning - Volume 37, ICML '15*, pp. 2143–2151, Lille, France, July 2015. JMLR.org.

-
- Spencer Churchill and Brian Chao. Anime face dataset, 2019. URL <https://www.kaggle.com/ds/379764>.
- Tarin Clanuwat, Mikel Bober-Irizar, Asanobu Kitamoto, Alex Lamb, Kazuaki Yamamoto, and David Ha. Deep learning for classical japanese literature. *arXiv preprint arXiv:1812.01718*, 2018.
- J. R. Clough, N. Byrne, I. Oksuz, V. A. Zimmer, J. A. Schnabel, and A. P. King. A topological loss function for deep-learning based image segmentation using persistent homology. *IEEE Transactions on Pattern Analysis & Machine Intelligence*, 44(12):8766–8778, December 2022. ISSN 1939-3539. doi: 10.1109/TPAMI.2020.3013679.
- Marco Cuturi. Sinkhorn distances: Lightspeed computation of optimal transport. *Advances in neural information processing systems*, 26, 2013.
- Asha Das, Vinod Kumar Devarampati, and Madhu S Nair. Nas-sgan: a semi-supervised generative adversarial network model for atypia scoring of breast cancer histopathological images. *IEEE Journal of Biomedical and Health Informatics*, 26(5):2276–2287, 2021.
- Colin Decourt and Luc Duong. Semi-supervised generative adversarial networks for the segmentation of the left ventricle in pediatric mri. *Computers in Biology and Medicine*, 123:103884, 2020.
- Tamal Krishna Dey and Yusu Wang. *Computational Topology for Data Analysis*. Cambridge University Press, March 2022. ISBN 978-1-00-910319-0.
- J. Dieudonne. *Foundations of Modern Analysis*. Academic Press, New York, 1969. ISBN 978-1-4465-4751-9.
- Vincent Divol and Théo Lacombe. Understanding the topology and the geometry of the space of persistence diagrams via optimal partial transport. *J. Appl. Comput. Topol.*, 5(1):1–53, March 2021. ISSN 2367-1734. doi: 10.1007/s41468-020-00061-z.
- Vincent Divol and Wolfgang Polonik. On the choice of weight functions for linear representations of persistence diagrams. *J. Appl. Comput. Topol.*, 3(3):249–283, September 2019. ISSN 2367-1734. doi: 10.1007/s41468-019-00032-z.
- Herbert Edelsbrunner and John L. Harer. *Computational Topology: An Introduction*. American Mathematical Society, 2010. ISBN 978-1-4704-6769-2.
- Chad Giusti and Darrick Lee. Signatures, lipschitz-free spaces, and paths of persistence diagrams. *SIAM Journal on Applied Algebra and Geometry*, 7(4):828–866, 2023. doi: 10.1137/22M1528471.
- Mario Gómez and Facundo Mémoli. Curvature Sets Over Persistence Diagrams. *Discrete & Computational Geometry*, 72(1):91–180, July 2024. ISSN 1432-0444. doi: 10.1007/s00454-024-00634-0.
- Ian Goodfellow, Jean Pouget-Abadie, Mehdi Mirza, Bing Xu, David Warde-Farley, Sherjil Ozair, Aaron Courville, and Yoshua Bengio. Generative adversarial nets. *Advances in neural information processing systems*, 27, 2014.
- Arthur Gretton, Karsten M. Borgwardt, Malte J. Rasch, Bernhard Schölkopf, and Alexander Smola. A kernel two-sample test. *J. Mach. Learn. Res.*, 13:723–773, March 2012. ISSN 1533-7928.
- Ishaan Gulrajani, Faruk Ahmed, Martin Arjovsky, Vincent Dumoulin, and Aaron C Courville. Improved training of wasserstein gans. *Advances in neural information processing systems*, 30, 2017.
- Felix Hensel, Michael Moor, and Bastian Rieck. A Survey of Topological Machine Learning Methods. *Frontiers in Artificial Intelligence*, 4, May 2021. ISSN 2624-8212. doi: 10.3389/frai.2021.681108.
- Martin Heusel, Hubert Ramsauer, Thomas Unterthiner, Bernhard Nessler, and Sepp Hochreiter. Gans trained by a two time-scale update rule converge to a local nash equilibrium. *Advances in neural information processing systems*, 30, 2017.

-
- Danijela Horak, Simiao Yu, and Gholamreza Salimi-Khorshidi. Topology Distance: A Topology-Based Approach for Evaluating Generative Adversarial Networks. *Proceedings of the AAAI Conference on Artificial Intelligence*, 35(9):7721–7728, May 2021. ISSN 2374-3468. doi: 10.1609/aaai.v35i9.16943.
- Max Horn, Edward De Brouwer, Michael Moor, Yves Moreau, Bastian Rieck, and Karsten Borgwardt. Topological Graph Neural Networks. In *International Conference on Learning Representations*, October 2021.
- Xiaoling Hu, Fuxin Li, Dimitris Samaras, and Chao Chen. Topology-Preserving Deep Image Segmentation. In *Advances in Neural Information Processing Systems*, volume 32. Curran Associates, Inc., 2019.
- Sadeep Jayasumana, Srikumar Ramalingam, Andreas Veit, Daniel Glasner, Ayan Chakrabarti, and Sanjiv Kumar. Rethinking fid: Towards a better evaluation metric for image generation. In *Proceedings of the IEEE/CVF Conference on Computer Vision and Pattern Recognition*, pp. 9307–9315, 2024.
- Kai Katsumata, Duc Minh Vo, Bei Liu, and Hideki Nakayama. Revisiting latent space of gan inversion for robust real image editing. In *Proceedings of the IEEE/CVF Winter Conference on Applications of Computer Vision*, pp. 5313–5322, 2024.
- Valentin Khrulkov and Ivan Oseledets. Geometry score: A method for comparing generative adversarial networks. In Jennifer Dy and Andreas Krause (eds.), *Proceedings of the 35th International Conference on Machine Learning*, volume 80 of *Proceedings of Machine Learning Research*, pp. 2621–2629. PMLR, 2018.
- Genki Kusano, Yasuaki Hiraoka, and Kenji Fukumizu. Persistence weighted Gaussian kernel for topological data analysis. In Maria-Florina Balcan and Kilian Q. Weinberger (eds.), *Proceedings of the 33rd International Conference on Machine Learning*, volume 48 of *JMLR Workshop and Conference Proceedings*, pp. 2004–2013. JMLR.org, 2016.
- AIDOS Lab. Pytorch-topological: A topological machine learning framework for pytorch. <https://github.com/aidos-lab/pytorch-topological?tab=readme-ov-file>.
- Théo Lacombe, Marco Cuturi, and Steve Oudot. Large scale computation of means and clusters for persistence diagrams using optimal transport. *Advances in Neural Information Processing Systems*, 31, 2018.
- Jacob Leygonie, Steve Oudot, and Ulrike Tillmann. A Framework for Differential Calculus on Persistence Barcodes. *Foundations of Computational Mathematics*, 22(4):1069–1131, August 2022. ISSN 1615-3383. doi: 10.1007/s10208-021-09522-y.
- Tengyuan Liang and James Stokes. Interaction matters: A note on non-asymptotic local convergence of generative adversarial networks. In *The 22nd International Conference on Artificial Intelligence and Statistics*, pp. 907–915. PMLR, 2019.
- Wei-An Lin, Chun Pong Lau, Alexander Levine, Rama Chellappa, and Soheil Feizi. Dual manifold adversarial robustness: Defense against lp and non-lp adversarial attacks. *Advances in Neural Information Processing Systems*, 33:3487–3498, 2020.
- Ziwei Liu, Ping Luo, Xiaogang Wang, and Xiaoou Tang. Deep learning face attributes in the wild. In *Proceedings of the IEEE international conference on computer vision*, pp. 3730–3738, 2015.
- Mingsheng Long, Han Zhu, Jianmin Wang, and Michael I Jordan. Deep transfer learning with joint adaptation networks. In *International conference on machine learning*, pp. 2208–2217. PMLR, 2017.
- Ilya Loshchilov and Frank Hutter. Sgdr: Stochastic gradient descent with warm restarts. *arXiv preprint arXiv:1608.03983*, 2016.
- Yuan Luo and Bradley J. Nelson. Accelerating iterated persistent homology computations with warm starts. *Computational Geometry*, 120:102089, June 2024. ISSN 0925-7721. doi: 10.1016/j.comgeo.2024.102089.

-
- Divyam Madaan, Jinwoo Shin, and Sung Ju Hwang. Adversarial neural pruning with latent vulnerability suppression. In *International Conference on Machine Learning*, pp. 6575–6585. PMLR, 2020.
- Arnab Kumar Mondal, Piyush Tiwary, Parag Singla, and AP Prathosh. Few-shot cross-domain image generation via inference-time latent-code learning. In *The Eleventh International Conference on Learning Representations*, 2023.
- Krikamol Muandet, Kenji Fukumizu, Bharath Sriperumbudur, and Bernhard Schölkopf. *Kernel Mean Embedding of Distributions: A Review and Beyond*. 2017. doi: 10.1561/22000000060.
- Arnur Nigmatov and Dmitriy Morozov. Topological Optimization with Big Steps. *Discrete & Computational Geometry*, 72(1):310–344, July 2024. ISSN 1432-0444. doi: 10.1007/s00454-023-00613-x.
- Partha Niyogi. Manifold regularization and semi-supervised learning: Some theoretical analyses. *Journal of Machine Learning Research*, 14(5), 2013.
- Maxime Oquab, Timothée Darcet, Théo Moutakanni, Huy Vo, Marc Szafraniec, Vasil Khalidov, Pierre Fernandez, Daniel Haziza, Francisco Massa, Alaaeldin El-Nouby, et al. Dinov2: Learning robust visual features without supervision. *Transactions on Machine Learning Research Journal*, pp. 1–31, 2024.
- Nina Otter, Mason A. Porter, Ulrike Tillmann, Peter Grindrod, and Heather A. Harrington. A roadmap for the computation of persistent homology. *EPJ Data Sci.*, 6(1):1–38, December 2017. ISSN 2193-1127. doi: 10.1140/epjds/s13688-017-0109-5.
- Theodore Papamarkou, Tolga Birdal, Michael M. Bronstein, Gunnar E. Carlsson, Justin Curry, Yue Gao, Mustafa Hajji, Roland Kwitt, Pietro Lio, Paolo Di Lorenzo, Vasileios Maroulas, Nina Miolane, Farzana Nasrin, Karthikeyan Natesan Ramamurthy, Bastian Rieck, Simone Scardapane, Michael T Schaub, Petar Veličković, Bei Wang, Yusu Wang, Guowei Wei, and Ghada Zamzmi. Position: Topological deep learning is the new frontier for relational learning. In *Forty-first International Conference on Machine Learning*, 2024. URL <https://openreview.net/forum?id=N13RG5XWAt>.
- Julián Burella Pérez, Sydney Hauke, Umberto Lupo, Matteo Caorsi, and Alberto Dassatti. Giotto-ph: A Python Library for High-Performance Computation of Persistent Homology of Vietoris-Rips Filtrations, August 2021.
- Alec Radford, Jong Wook Kim, Chris Hallacy, Aditya Ramesh, Gabriel Goh, Sandhini Agarwal, Girish Sastry, Amanda Askell, Pamela Mishkin, Jack Clark, et al. Learning transferable visual models from natural language supervision. In *International conference on machine learning*, pp. 8748–8763. PMLR, 2021.
- Edgar Schonfeld, Sayna Ebrahimi, Samarth Sinha, Trevor Darrell, and Zeynep Akata. Generalized zero-and few-shot learning via aligned variational autoencoders. In *Proceedings of the IEEE/CVF conference on computer vision and pattern recognition*, pp. 8247–8255, 2019.
- Luis Scoccola, Siddharth Setlur, David Loiseaux, Mathieu Carrière, and Steve Oudot. Differentiability and Optimization of Multiparameter Persistent Homology. In *Proceedings of the 41st International Conference on Machine Learning*, pp. 43986–44011. PMLR, July 2024.
- Suprosanna Shit, Johannes C. Paetzold, Anjany Sekuboyina, Ivan Ezhov, Alexander Unger, Andrey Zhylka, Josien P. W. Pluim, Ulrich Bauer, and Bjoern H. Menze. cIDice - a Novel Topology-Preserving Loss Function for Tubular Structure Segmentation. In *2021 IEEE/CVF Conference on Computer Vision and Pattern Recognition (CVPR)*, pp. 16555–16564, June 2021. doi: 10.1109/CVPR46437.2021.01629.
- Carl-Johann Simon-Gabriel and Bernhard Schölkopf. Kernel distribution embeddings: Universal kernels, characteristic kernels and kernel metrics on distributions. *J. Mach. Learn. Res.*, 19(44): 1–29, 2018. ISSN 1533-7928.

-
- Carl-Johann Simon-Gabriel, Alessandro Barp, Bernhard Schölkopf, and Lester Mackey. Metrizing Weak Convergence with Maximum Mean Discrepancies. *Journal of Machine Learning Research*, 24(184):1–20, 2023. ISSN 1533-7928.
- Elchanan Solomon, Alexander Wagner, and Paul Bendich. From geometry to topology: Inverse theorems for distributed persistence. In Xavier Goaoc and Michael Kerber (eds.), *38th International Symposium on Computational Geometry (SoCG 2022)*, volume 224 of *Leibniz International Proceedings in Informatics (LIPIcs)*, pp. 61:1–61:16, Dagstuhl, Germany, 2022. Schloss Dagstuhl – Leibniz-Zentrum für Informatik. ISBN 978-3-95977-227-3. doi: 10.4230/LIPIcs.SoCG.2022.61.
- Yitzchak Solomon, Alexander Wagner, and Paul Bendich. A Fast and Robust Method for Global Topological Functional Optimization. In *Proceedings of The 24th International Conference on Artificial Intelligence and Statistics*, pp. 109–117. PMLR, March 2021.
- Bharath Sriperumbudur. On the optimal estimation of probability measures in weak and strong topologies. *Bernoulli*, 22(3):1839–1893, August 2016. ISSN 1350-7265. doi: 10.3150/15-BEJ713.
- George Stein, Jesse Cresswell, Rasa Hosseinzadeh, Yi Sui, Brendan Ross, Valentin Vilecroze, Zhaoyan Liu, Anthony L Caterini, Eric Taylor, and Gabriel Loaiza-Ganem. Exposing flaws of generative model evaluation metrics and their unfair treatment of diffusion models. *Advances in Neural Information Processing Systems*, 36, 2024.
- Bernadette J. Stolz. Outlier-Robust Subsampling Techniques for Persistent Homology. *Journal of Machine Learning Research*, 24(90):1–35, 2023. ISSN 1533-7928.
- Baochen Sun and Kate Saenko. Deep coral: Correlation alignment for deep domain adaptation. In *Computer Vision—ECCV 2016 Workshops: Amsterdam, The Netherlands, October 8-10 and 15-16, 2016, Proceedings, Part III 14*, pp. 443–450. Springer, 2016.
- Baochen Sun, Jiashi Feng, and Kate Saenko. Return of frustratingly easy domain adaptation. In *Proceedings of the AAAI conference on artificial intelligence*, volume 30, 2016.
- Álvaro Torras-Casas. Distributing Persistent Homology via Spectral Sequences. *Discrete & Computational Geometry*, 70(3):580–619, October 2023. ISSN 1432-0444. doi: 10.1007/s00454-023-00549-2.
- Nhan Duy Truong, Luping Zhou, and Omid Kavehei. Semi-supervised seizure prediction with generative adversarial networks. In *2019 41st annual international conference of the IEEE engineering in medicine and biology society (EMBC)*, pp. 2369–2372. IEEE, 2019.
- Cédric Villani. *Optimal Transport: Old and New*. Grundlehren Der Mathematischen Wissenschaften. Springer-Verlag, Berlin Heidelberg, 2009. ISBN 978-3-540-71049-3. doi: 10.1007/978-3-540-71050-9.
- Dominik J. E. Waibel, Scott Atwell, Matthias Meier, Carsten Marr, and Bastian Rieck. Capturing Shape Information with Multi-scale Topological Loss Terms for 3D Reconstruction. In Linwei Wang, Qi Dou, P. Thomas Fletcher, Stefanie Speidel, and Shuo Li (eds.), *Medical Image Computing and Computer Assisted Intervention – MICCAI 2022*, Lecture Notes in Computer Science, pp. 150–159, Cham, 2022. Springer Nature Switzerland. ISBN 978-3-031-16440-8. doi: 10.1007/978-3-031-16440-8_15.
- Lei Wang, Xin Yan, Zhu-Hong You, Xi Zhou, Hao-Yuan Li, and Yu-An Huang. Sganrda: semi-supervised generative adversarial networks for predicting circrna–disease associations. *Briefings in Bioinformatics*, 22(5):bbab028, 2021a.
- Zijian Wang, Yadan Luo, Ruihong Qiu, Zi Huang, and Mahsa Baktashmotlagh. Learning to diversify for single domain generalization. In *Proceedings of the IEEE/CVF International Conference on Computer Vision*, pp. 834–843, 2021b.
- Maciej Wiatrak, Stefano V Albrecht, and Andrew Nystrom. Stabilizing generative adversarial networks: A survey. *arXiv preprint arXiv:1910.00927*, 2019.
- H Xiao. Fashion-mnist: a novel image dataset for benchmarking machine learning algorithms. *arXiv preprint arXiv:1708.07747*, 2017.

-
- Jian Xu, Bo Liu, and Yanshan Xiao. A multitask latent feature augmentation method for few-shot learning. *IEEE Transactions on neural networks and learning systems*, 2022.
- Ruijia Xu, Guanbin Li, Jihan Yang, and Liang Lin. Larger norm more transferable: An adaptive feature norm approach for unsupervised domain adaptation. In *Proceedings of the IEEE/CVF international conference on computer vision*, pp. 1426–1435, 2019.
- Xiangli Yang, Zixing Song, Irwin King, and Zenglin Xu. A survey on deep semi-supervised learning. *IEEE Transactions on Knowledge and Data Engineering*, 35(9):8934–8954, 2022.
- Hee Rhang Yoon and Robert Ghrist. Persistence by parts: Multiscale feature detection via distributed persistent homology. *arXiv: 2001.01623*, 2020.
- Fisher Yu, Ari Seff, Yinda Zhang, Shuran Song, Thomas Funkhouser, and Jianxiong Xiao. Lsun: Construction of a large-scale image dataset using deep learning with humans in the loop. *arXiv preprint arXiv:1506.03365*, 2015.
- Yunrui Yu, Xitong Gao, and Cheng-Zhong Xu. Lfeat: Piercing through adversarial defenses with latent features. In *Proceedings of the IEEE/CVF conference on computer vision and pattern recognition*, pp. 5735–5745, 2021.
- Simon Zhang, Mengbai Xiao, and Hao Wang. GPU-Accelerated Computation of Vietoris-Rips Persistence Barcodes. In *DROPS-IDN/v2/Document/10.4230/LIPIcs.SoCG.2020.70*. Schloss Dagstuhl – Leibniz-Zentrum für Informatik, 2020. doi: 10.4230/LIPIcs.SoCG.2020.70.
- Kaiyang Zhou, Yongxin Yang, Timothy Hospedales, and Tao Xiang. Learning to generate novel domains for domain generalization. In *Computer Vision–ECCV 2020: 16th European Conference, Glasgow, UK, August 23–28, 2020, Proceedings, Part XVI 16*, pp. 561–578. Springer, 2020.
- Sharon Zhou, Eric Zelikman, Fred Lu, Andrew Y. Ng, Gunnar E. Carlsson, and Stefano Ermon. Evaluating the disentanglement of deep generative models through manifold topology. In *International Conference on Learning Representations*, 2021.
- Jiapeng Zhu, Ceyuan Yang, Kecheng Zheng, Yinghao Xu, Zifan Shi, and Yujun Shen. Exploring sparse moe in gans for text-conditioned image synthesis. *arXiv preprint arXiv:2309.03904*, 2023.

A BACKGROUND ON KERNELS AND MMD

In this section, we provide a brief overview of kernel methods, leading towards the maximum mean discrepancy. For further background, we refer the reader to (Muandet et al., 2017).

Kernels and Feature Maps Suppose \mathcal{X} is a topological space on which we wish to study either functions $f : \mathcal{X} \rightarrow \mathbb{R}$ or measures $\mu \in \mathcal{P}(\mathcal{X})$. A common way to consider such objects is by using a *feature map*

$$\Phi : \mathcal{X} \rightarrow \mathcal{H} \quad (17)$$

into some Hilbert space \mathcal{H} . Heuristically, we can consider

- **functions on \mathcal{X}** via linear functionals $\langle \ell, \Phi(\cdot) \rangle_{\mathcal{H}} : \mathcal{X} \rightarrow \mathbb{R}$ where $\ell \in \mathcal{H}$, and
- **measures on \mathcal{X}** by considering the *kernel mean embedding* (which we also denote by Φ), defined by

$$\Phi : \mathcal{P}(\mathcal{X}) \rightarrow \mathcal{H}, \quad \Phi(\mu) = \int_{\mathcal{X}} \Phi(x) d\mu(x). \quad (18)$$

Given this feature map, we can define a positive-definite *kernel* $k : \mathcal{X} \times \mathcal{X} \rightarrow \mathbb{R}$ defined by

$$k(x, y) := \langle \Phi(x), \Phi(y) \rangle_{\mathcal{H}}. \quad (19)$$

Reproducing Kernel Hilbert Spaces. In fact, we can also go in the other direction and start with a continuous positive definite kernel $k : \mathcal{X} \times \mathcal{X} \rightarrow \mathbb{R}$, and obtain a feature map from \mathcal{X} into a Hilbert space of functions. In particular, we define \mathcal{H} to be the completion of the linear span of functions $\{k(x, \cdot) : \mathcal{X} \rightarrow \mathbb{R} : x \in \mathcal{X}\}$, equipped with the inner product

$$\langle k(x, \cdot), k(y, \cdot) \rangle := k(x, y). \quad (20)$$

By the Moore-Aronszajn theorem (Aronszajn, 1950), \mathcal{H} is a Hilbert space with the *reproducing kernel* property: for any $f \in \mathcal{H}$ and $x \in \mathcal{X}$, we have

$$\langle f, k(x, \cdot) \rangle = f(x). \quad (21)$$

Thus, \mathcal{H} is a *reproducing kernel Hilbert space (RKHS)*. Note that this is a Hilbert space of functions, $\mathcal{H} \subset C(\mathcal{X}, \mathbb{R})$. Then, we can define a feature map $\Phi : \mathcal{X} \rightarrow \mathcal{H}$ by

$$\Phi(x) := k(x, \cdot). \quad (22)$$

Universality and Characteristicness We wish to consider feature maps (or kernels) which satisfy additional properties such that they can approximate functions and characterize measures. Let $\mathcal{F} \subset C(\mathcal{X}, \mathbb{R})$ be a topological vector space, and suppose \mathcal{M} is a space of measures on \mathcal{X} . A feature map $\Phi : \mathcal{X} \rightarrow \mathcal{H}$ (with associated kernel $k : \mathcal{X} \times \mathcal{X} \rightarrow \mathbb{R}$), where $\mathcal{H} \subset \mathcal{F}$ is (Simon-Gabriel & Schölkopf, 2018)

- **universal** with respect to \mathcal{F} if \mathcal{H} is dense in \mathcal{F} (we can approximate functions in \mathcal{F} using functions in \mathcal{H}); and
- **characteristic** with respect to \mathcal{M} if the kernel mean embedding in Equation (18) is injective.

Maximum Mean Discrepancy Given a feature map $\Phi : \mathcal{X} \rightarrow \mathcal{H}$ (with kernel k) characteristic to the space of probability measures $\mathcal{P}(\mathcal{X})$, we can use the Hilbert space norm to define a metric on this space of measures. In fact, this is equivalent to the notion of *maximum mean discrepancy (MMD)* from statistics. In particular, given a function class $\mathcal{F} \subset C(\mathcal{X}, \mathbb{R})$, we define the MMD with respect to \mathcal{F} by

$$\text{MMD}_{\mathcal{F}}(\mu, \nu) := \sup_{f \in \mathcal{F}} (\mathbb{E}_{x \sim \mu}[f(x)] - \mathbb{E}_{y \sim \nu}[f(y)]). \quad (23)$$

Now, by (Gretton et al., 2012, Lemma 4), if we choose \mathcal{F} to be the unit ball of the RKHS \mathcal{H} (with respect to a characteristic kernel k), the MMD with respect to \mathcal{F} is exactly the Hilbert space norm,

$$\text{MMD}_{\mathcal{F}}(\mu, \nu) = \|\Phi(\mu) - \Phi(\nu)\|_{\mathcal{H}} =: \text{MMD}_k(\mu, \nu), \quad (24)$$

where the right hand side is how we define MMD_k in Equation (11).

B CHARACTERISTIC KERNELS ON Ω .

In this appendix, we provide a detailed discussion of the proof of Theorem 1.

We begin by characterizing some of the elements in the RKHS \mathcal{H}_Ω .

Lemma 1. *The RKHS \mathcal{H}_Ω satisfies*

$$\mathcal{H}_\Omega \supset \{g : \Omega \rightarrow \mathbb{R} : g(b, \ell) = \ell \cdot f(b, \ell), f \in \mathcal{H}\}. \quad (25)$$

Proof. By Moore-Aronszajn (Aronszajn, 1950), an element of $g \in \mathcal{H}_\Omega$ is defined by a convergent series

$$g(b, \ell) = \sum_{i=1}^{\infty} c_i k_\Omega((b_i, \ell_i), (b, \ell)) = \ell \sum_{i=1}^{\infty} c_i \ell_i k((b_i, \ell_i), (b, \ell)) = \ell \cdot f(b, \ell), \quad (26)$$

where $f(b, \ell) = \sum_{i=1}^{\infty} c_i \ell_i k((b_i, \ell_i), (b, \ell))$. Note that if the coefficient series for f given by $\sum_{i=1}^{\infty} |c_i| \ell_i k((b_i, \ell_i), (b_i, \ell_i))$ is convergent, then the coefficient series for g given by

$$\sum_{i=1}^{\infty} |c_i| k_\Omega((b_i, \ell_i), (b_i, \ell_i)) = \sum_{i=1}^{\infty} |c_i| \ell_i^2 k((b_i, \ell_i), (b_i, \ell_i)) \leq T \sum_{i=1}^{\infty} |c_i| \ell_i k((b_i, \ell_i), (b_i, \ell_i)) \quad (27)$$

is also convergent, since $\ell_i \leq T$. \square

Universality and Characteristicness. Our first main result concerns the transfer of universal and characteristic properties from k to k_Ω . First, we define the space of *linear-growth continuous functions* on Ω_T by

$$C_{\text{lin}}(\Omega_T) := \{\ell \cdot f(b, \ell) \in C(\Omega_T) : f(b, \ell) \in C([0, T]^2)\}, \quad (28)$$

where we equip it with the norm defined on $g = \ell \cdot f$ by

$$\|g\|_{\text{lin}} := |f|_\infty. \quad (29)$$

Note that for all $g \in C_{\text{lin}}(\Omega)$ have the property that $g(*) = 0$, and $(C_{\text{lin}}(\Omega_T), \|\cdot\|_{\text{lin}})$ and $(C([0, T]^2), |\cdot|_\infty)$ are isometric Banach spaces.

Theorem 4. *Let $k : [0, T]^2 \times [0, T]^2 \rightarrow \mathbb{R}$ be a kernel on $[0, T]^2$ universal to $C([0, T]^2)$. Then, $k_\Omega : \Omega \times \Omega \rightarrow \mathbb{R}$ is universal with respect to $C_{\text{lin}}(\Omega_T)$.*

Proof. Let $g \in C_{\text{lin}}(\Omega_T)$ and suppose $g = \ell \cdot f$ for some $f \in C([0, T]^2)$. Because k is universal, there exists $f_n \in \mathcal{H}$ such that $|f_n - f|_\infty \rightarrow 0$. Then, by Lemma 1, $g_n = \ell \cdot f_n \in \mathcal{H}_\Omega$, and furthermore, by the definition of $\|\cdot\|_{\text{lin}}$ in Equation (29), we have $\|g_n - g\|_{\text{lin}} \rightarrow 0$. Thus, k_Ω is universal with respect to $C_{\text{lin}}(\Omega_T)$. \square

The main result we wish to obtain is characteristicness with respect to measures on Ω . We begin by applying the duality theorem of (Simon-Gabriel & Schölkopf, 2018, Theorem 6) which immediately implies characteristicness with respect to the topological dual of $C_{\text{lin}}(\Omega)$, which we equip with the weak-* topology with respect to $C_{\text{lin}}(\Omega)$.

Corollary 1. *Let $k : [0, T]^2 \times [0, T]^2 \rightarrow \mathbb{R}$ be a kernel on $[0, T]^2$ universal to $C([0, T]^2)$. Then, k_Ω is characteristic with respect to $C_{\text{lin}}(\Omega)^*$.*

Our next task is to show that our desired measures are contained in this dual space.

Theorem 5. *Let $q : [0, T]^2 \rightarrow \Omega$ denote the quotient map, and let $s : [0, T]^2 \rightarrow [0, \infty)$ be defined by $s(b, \ell) = \ell$ for $\ell > 0$ and $s(b, 0) = 0$. Define*

$$\mathcal{M}_{\text{lin}}(\Omega) := \left\{ q_* \mu \in \mathcal{M}(\Omega) : \mu \in \mathcal{M}([0, T]^2), \mu(\{\ell = 0\}) = 0, \left| \int_{[0, T]^2} \ell d\mu \right| < \infty \right\}, \quad (30)$$

then $\mathcal{M}_{\text{lin}}(\Omega) \subset C_{\text{lin}}(\Omega)^*$.

Proof. Let $q_*\mu \in \mathcal{M}_{\text{lin}}(\Omega)$. Then, for $g = \ell \cdot f \in C_{\text{lin}}(\Omega)$, we have

$$\left| \int_{\Omega} \ell \cdot f(b, \ell) q_* d\nu \right| = \left| \int_{[0, T]^2} \ell \cdot f(b, \ell) d\mu \right| \leq \|g\|_{\text{lin}} \left| \int_{[0, T]^2} \ell d\mu \right|, \quad (31)$$

where we use $\mu(\{\ell = 0\}) = 0$ in the first equality. Thus, $q_*\mu$ is a bounded (hence continuous) linear functional. \square

As we wish to use this kernel to study PPMs, we are interested in probability measures on Ω . However, the elements in the dual only contain measures which are trivial on $* \in \Omega$ (whereas PPMs may have nontrivial mass on $*$), and thus we first define a different representation of probability measures. In particular, we define

$$\mathcal{P}_{\text{lin}}(\Omega) := \{\nu \in \mathcal{M}_{\text{lin}}(\Omega) : |\nu| \leq 1\} = \{\nu \in \mathcal{M}(\Omega) : \nu(\{*\}) = 0, |\nu| \leq 1\} \subset \mathcal{M}_{\text{lin}}(\Omega). \quad (32)$$

Note that the equality holds since the moment condition in Equation (30) is immediately satisfied since the measures are finite with bounded support. With the following two lemmas, we show that this coincides with $\mathcal{P}(\Omega)$.

Lemma 2. *The space $C_{\text{lin}}(\Omega)$ is dense in $C_0(\Omega)$ equipped with the uniform topology.*

Proof. Let $g \in C_0(\Omega)$, and since g is uniformly continuous (since Ω is compact) and $g(*) = 0$, for every $\epsilon > 0$, there exists some ℓ_ϵ such that $g(b, \ell) < \epsilon$ whenever $\ell < \ell_\epsilon$. Now, define $f_n \in C([0, T]^2)$ by

$$f_n(b, \ell) = \frac{g(b, \ell)}{\ell} \quad \text{for } \ell \geq \ell_{1/n} \quad \text{and} \quad f_n(b, \ell) = \frac{g(b, \ell_{1/n})}{\ell_{1/n}} \quad \text{for } \ell < \ell_{1/n}. \quad (33)$$

Then, define $g_n(b, \ell) = \ell \cdot f(b, \ell)$, where $g_n(b, \ell) = g(b, \ell)$ whenever $\ell \geq \ell_{1/n}$. When $\ell < \ell_{1/n}$, we have

$$|g_n(b, \ell) - g(b, \ell)| = |g_n(b, \ell_{1/n}) - g(b, \ell)| \leq \frac{2}{n}, \quad (34)$$

so g_n converges uniformly to g . \square

Lemma 3. *There exists a homeomorphism*

$$\psi : \mathcal{P}(\Omega) \rightarrow \mathcal{P}_{\text{lin}}(\Omega) \quad (35)$$

where $\mathcal{P}(\Omega)$ is equipped with the weak-* topology with respect to $C(\Omega)$ and $\mathcal{P}_{\text{lin}}(\Omega)$ is equipped with the weak-* topology with respect to $C_{\text{lin}}(\Omega)$.

Proof. We define ψ and its inverse by

$$\psi(\mu) := \mu - \mu(*)\delta_* \quad \text{and} \quad \psi^{-1}(\nu) = \nu + (1 - \nu(\Omega))\delta_*, \quad (36)$$

where δ_* denotes the Dirac measure on $* \in \Omega$. By definition of $\mathcal{P}_{\text{lin}}(\Omega)$ in Equation (32), this map is a bijection. It remains to show that $\mu_n \rightarrow \mu$ in $\mathcal{P}(\Omega)$ if and only if $\psi(\mu_n) \rightarrow \psi(\mu)$ in $\mathcal{P}_{\text{lin}}(\Omega)$.

Note that for any $f \in C(\Omega)$ and $\mu \in \mathcal{P}(\Omega)$, we can decompose the integral as

$$\mu(f) = \int_{\Omega} f d\mu = \int_{\Omega - \{*\}} f d\mu + f(*)\mu(\{*\}). \quad (37)$$

Then, for $f \in C_{\text{lin}}(\Omega)$, we have

$$\mu(f) = \int_{\Omega - \{*\}} f d\mu = \int_{\Omega - \{*\}} f d\psi(\mu) \quad (38)$$

since $f(*) = 0$ and $\mu = \psi(\mu)$ on $\Omega - \{*\}$. Thus, if $\mu_n \rightarrow \mu$ in $\mathcal{P}(\Omega)$ then $\psi(\mu_n) \rightarrow \psi(\mu)$ in $\mathcal{P}_{\text{lin}}(\Omega)$.

Next, suppose that $\nu_n \rightarrow \nu$ in $\mathcal{P}_{\text{lin}}(\Omega)$. Now, we note that $\mathcal{P}_{\text{lin}}(\Omega) \subset \mathcal{M}(\Omega)$, and thus are also continuous functionals on $C(\Omega)$ with respect to the uniform topology. By Lemma 2, we have $\nu_n(f) \rightarrow \nu(f)$ for all $f \in C_0(\Omega)$. However, this also implies it holds for all $f \in C(\Omega)$, since

we obtain functions in $C(\Omega)$ by adding a constant to a function in $C_0(\Omega)$ and $\nu(\{*\}) = 0$ for all $\nu \in \mathcal{P}_{\text{lin}}(\Omega)$. This implies that

$$\int_{\Omega - \{*\}} f d\psi^{-1}(\nu_n) \rightarrow \int_{\Omega - \{*\}} f d\psi^{-1}(\nu) \quad (39)$$

since $\nu = \psi^{-1}(\nu)$ on $\Omega - \{*\}$ for all $\nu \in \mathcal{P}_{\text{lin}}(\Omega)$. Furthermore, this implies that $\nu_n(\Omega) \rightarrow \nu(\Omega)$, and thus by definition of ψ^{-1} in Equation (36), we have $\psi^{-1}(\nu_n) \rightarrow \psi^{-1}(\nu)$ in $\mathcal{P}(\Omega)$. \square

This result allows us to work with $\mathcal{P}(\Omega)$ and $\mathcal{P}_{\text{lin}}(\Omega)$ interchangeably. In particular, note that $\Phi_\Omega(*) = 0 \in \mathcal{H}_\Omega$. This implies that for any $\mu \in \mathcal{P}(\Omega)$, we have

$$\Phi_\Omega(\mu) = \Phi_\Omega(\psi(\mu)). \quad (40)$$

Proof of Theorem 1. By Corollary 1, k_Ω is characteristic with respect to $\mathcal{M}_{\text{lin}}(\Omega)$, and $\mathcal{P}_{\text{lin}}(\Omega) \subset \mathcal{M}_{\text{lin}}(\Omega)$ by Theorem 5. Next, by Lemma 3, we can apply the identity Equation (40) to conclude that k_Ω is characteristic with respect to $\mathcal{P}(\Omega)$. \square

C METRIZING WEAK TOPOLOGY

In this appendix, we provide a detailed discussion of the proof of Theorem 2.

Maximum Mean Discrepancy (MMD). Because k_Ω is a characteristic kernel on Ω , the *kernel mean embedding*, defined (by an abuse of notation) on $\nu = q_*\mu \in \mathcal{M}_{\text{lin}}(\Omega)$ by

$$\Phi_\Omega : \mathcal{M}_{\text{lin}}(\Omega) \rightarrow \mathcal{H}_\Omega, \quad \Phi(\nu) := \mathbb{E}_{z \sim \nu}[\Phi_\Omega(z)], \quad (41)$$

is injective. This induces a metric on $\mathcal{M}_{\text{lin}}(\Omega)$, called the *maximum mean discrepancy (MMD)*,

$$\text{MMD}_k(\nu_1, \nu_2) := \|\Phi(\nu_1) - \Phi(\nu_2)\|_{\mathcal{H}_\Omega}. \quad (42)$$

Our next result shows that the MMD metrizes the weak-* topology on $\mathcal{P}_{\text{lin}}(\Omega)$, where we can directly apply (Sriperumbudur, 2016, Theorem 3.2). See also (Simon-Gabriel et al., 2023) for related results.

Theorem 6. *The MMD metric metrizes the weak topology on $\mathcal{P}(\Omega)$. In other words, given measures $\nu_n, \nu \in \mathcal{P}(\Omega)$, we have $\text{MMD}_k(\nu_n, \nu) \rightarrow 0$ if and only if*

$$|\nu_n(g) - \nu(g)| \rightarrow 0 \quad (43)$$

for all $g \in C(\Omega)$.

Proof. This follows from (Sriperumbudur, 2016, Theorem 3.2) as Ω is a compact Polish space and k_Ω is a continuous bounded kernel. \square

Corollary 2. *The p -Wasserstein metric W_p and the MMD metric MMD_k induce the same topology on $\mathcal{P}(\Omega)$.*

Proof. This is a direct consequence of the above, since the p -Wasserstein distance also metrizes the weak topology on $\mathcal{P}(\Omega)$ (Villani, 2009, Theorem 6.9). \square

D PPM REGULARIZER HAS CONTINUOUS GRADIENTS

We say that a function $f : \mathbb{R}^n \rightarrow \mathbb{R}^m$ is a C^1 function if all first derivatives of f are continuous. We will begin with a more general statement which will immediately imply Theorem 3. Fix $\mu \in \mathcal{P}_c(\mathbb{R}^N)$ to be a measure, and let $h_\theta : \mathbb{R}^N \rightarrow \mathbb{R}^L$ be a mapping from \mathbb{R}^N to the latent space \mathbb{R}^L . Suppose that the mapping h_θ is parametrized by $\theta \in \mathbb{R}^P$, and define $H : \mathbb{R}^P \times \mathbb{R}^N \rightarrow \mathbb{R}^L$ by $H(\theta, x) = h_\theta(x)$. We aim to show that $\mathfrak{H} : \mathbb{R}^P \rightarrow \mathcal{H}_\Omega$, defined by

$$\mathfrak{H}(\theta) := \Phi_\Omega(\text{PPM}_q(h_\theta(\mu))) \quad (44)$$

is a smooth function. In particular, the pipeline for computing this feature map is

$$\mathcal{P}_c(\mathbb{R}^N) \xrightarrow{(h_\theta)_*} \mathcal{P}_c(\mathbb{R}^L) \xrightarrow{(-)^{\otimes(2k+2)}} \mathcal{P}_c((\mathbb{R}^L)^{2k+2}) \xrightarrow{(\text{PH}_k)_*} \mathcal{P}(\Omega) \xrightarrow{\Phi} \mathcal{H}, \quad (45)$$

Let $F : \mathbb{R}^P \rightarrow \mathcal{P}((\mathbb{R}^L)^{2k+2})$ be the map from the parameter space to the product measure in latent space. We assume that the resulting product measure has a C^1 density, which is true if H is C^1 , and μ has a C^1 density. Then, F has the form

$$F(\theta) = f(\theta, x)dx \quad (46)$$

where $f : \mathbb{R}^P \times (\mathbb{R}^L)^{2k+2} \rightarrow \mathbb{R}$ is a C^r function.

Theorem 7. *Let $\mu \in \mathcal{P}(\mathbb{R}^N)$ be a probability measure with a C^1 density, suppose $H : \mathbb{R}^P \times \mathbb{R}^N \rightarrow \mathbb{R}^L$ is a C^1 function. Then $\mathfrak{H} : \mathbb{R}^P \rightarrow \mathcal{H}_\Omega$ is a C^1 function (where derivatives are Fréchet derivatives).*

Proof. Expanding out the definition of \mathfrak{H} , we have

$$\Phi_\Omega(\text{PPM}_q(h_\theta(\mu))) = \int_\Omega \Phi_\Omega(z) d(\text{PH}_k)_* F(\theta)(z) \quad (47)$$

$$= \int_{(\mathbb{R}^L)^{2k+2}} \Phi_\Omega \circ \text{PH}_k(x) dF(\theta)(x) \quad (48)$$

$$= \int_{(\mathbb{R}^L)^{2k+2}} \Phi_\Omega \circ \text{PH}_k(x) f(\theta, x) dx, \quad (49)$$

where we use the definition of the pushforward in the second line, and the definition of the density of F in Equation (46). Now, this integral is a Bochner integral since it is valued in a Hilbert space, and we can still differentiate under the integral (by Hille’s theorem; see (Dieudonne, 1969, Paragraph 8.11.2)). Then, we have

$$\frac{\partial}{\partial \theta_i} \Phi_\Omega(\text{PPM}_q(h_\theta(\mu))) = \int_{(\mathbb{R}^L)^{2k+2}} \Phi_\Omega \circ \text{PH}_k(x) \frac{\partial f(\theta, x)}{\partial \theta_i} dx, \quad (50)$$

which is continuous since f is C^1 . □

Proof of Theorem 3. By direct application of Theorem 7, both

$$\theta \mapsto \Phi_\Omega \circ \text{PPM}_q \circ d_\theta(\mu) \quad \text{and} \quad (\theta, \omega) \mapsto \Phi_\Omega \circ \text{PPM}_q \circ d_\theta \circ g_\omega(\nu) \quad (51)$$

are C^1 functions. Then, since the norm is continuously differentiable away from the origin, we obtain the desired result. □

E SHAPE MATCHING

E.1 IMPLEMENTATION DETAILS FOR SHAPE MATCHING

Shape Matching Experiment. The task is to match the "shape" of two point clouds by optimizing a loss function of the form $\mathcal{L} + \mathcal{T}$ in ambient space. Throughout the experiment, we use gradient descent with momentum as the optimization algorithm. The value of the momentum parameter is 0.9 and the step size is 0.05. Two simple reference shapes in \mathbb{R}^2 are chosen for visualization purposes. They are a unit circle (left), and the union of two intersecting unit circles (right), shown in Figure 2. A noisy point cloud with 512 points is first initialized with a normally distributed at the origin with a standard deviation of 0.3, we call training shape. The reference shapes are also sampled as a point cloud with 512 points. The reference shape is fixed and the training shape changes towards the reference, guided by some loss function. We test for the effectiveness of four loss function, they are Cramer, MMD, Cramer + PPM-Reg and MMD + PPM-Reg. The MMD metric using an RBF kernel (with width $\sigma = 0.1$). Throughout the experiment, the hyperparameter of PPM-Reg is fixed as $\lambda = 1$, $\lambda_0 = 1$, $\lambda_1 = 6000$, $\sigma = 0.1$ and $s = 2000$. For Cramer + PPM-Reg, the weight of the cramer loss is 1.6. For MMD + PPM-Reg, the weight of the MMD loss is 5. In Figure 4, we show the the shapes after 16000 training steps. Even at this stage, we observe that there are several “leftover” points. This is partially due to the choice of the underlying loss functions, and we observe that in (b), (d) and (h), the trained shapes using PPM-Reg largely capture the topological features of the reference shape.

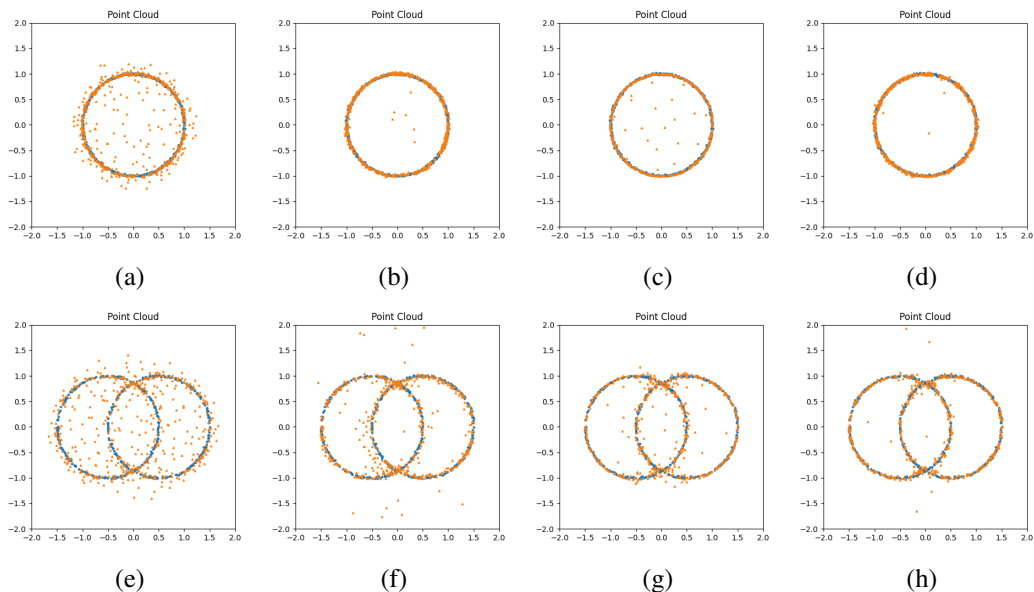


Figure 4: Plots of the shape matching experiment at convergence after 16000 steps. (a) and (e) use only the Cramer loss. (b) and (f) use Cramer + PPM-Reg. (c) and (g) use only the MMD loss. (d) and (h) use MMD + PPM-Reg.

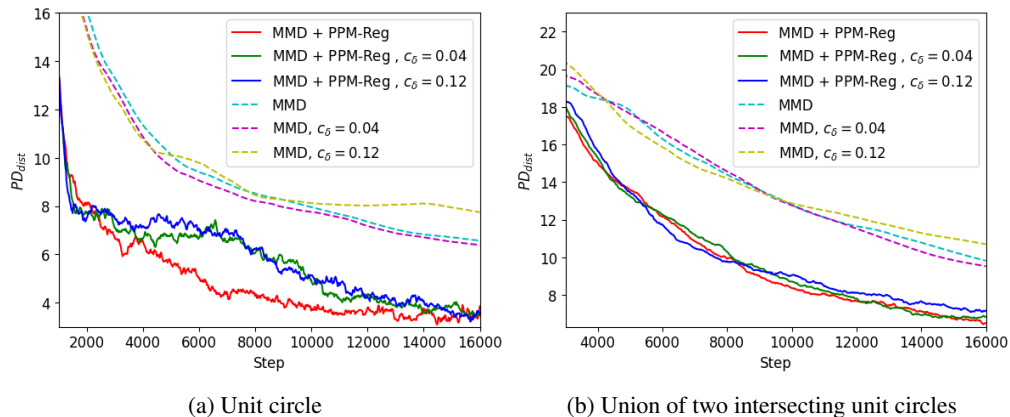


Figure 5: Illustrative example of the PPM-Reg in shape matching using MMD with increasing handicap contain. Plotting 2-Wasserstein distance upto 1-dimensional persistent homology between the reference shape and training shape (PD_{dist}) over optimization steps. The reference shape of (a) unit circle and (b) union of two intersecting unit circles. c_δ indicate the strength of the handicap (detail provided in Appendix E.2). Showing that the ability to matching topological features as the handicap contains increase.

Computational Comparison. Results are computed on Nvidia Geforce RTX 3060 with Intel Core i7-10700.

E.2 IMPERFECT CONVERGENCE

This section demonstrates the efficacy of PPM-Reg when the primary loss function \mathcal{L} is optimized imperfectly. As discussed in Section 1, most GAN training algorithms converge to a local saddle point. In simpler latent-space matching tasks, \mathcal{L} is often optimized alongside with other tasks. To summarize, converging to an imperfect \mathcal{L} value is a common occurrence in machine learning.

To restrict the solution of the shape matching problem, we impose a penalty term that prevents the centroid of the reference shapes and the training shape from being smaller than a user-defined value c_δ . The penalty term f_p is given by

$$f_p = \frac{\lambda_p}{\beta} \ln(1 + e^{\beta(c_\delta - \|c_{train} - c_{ref}\|_2)}), \quad (52)$$

where c_{train} and c_{ref} refers to the centroid of the training shape and reference shapes respectively. The term λ_p is the penalty strength, β is a tuning parameter. For the MMD case, $\mathcal{V} = \mathcal{L} + f_p$. For the MMD + PPM-Reg case, $\mathcal{V} = \mathcal{L} + \lambda\mathcal{T} + f_p$.

Implementation Details. We largely follow the setup on Section 6.2 and Appendix E.1, but make a few minor changes. We reduced the step size to 0.01 and performed 16,000 gradient steps. The hyperparameter of PPM-Reg is fixed as $\lambda = 1$, $\lambda_0 = 0.3$, $\lambda_1 = 6000$, $\sigma = 0.1$ and $s = 2000$. For the penalty function f_p , we set $\beta = 80$. The λ_p value remains the same when we vary c_δ and compare against adding PPM-Reg. The λ_p value is determined such that $\|c_{train} - c_{ref}\|_2$ converges to c_δ when $c_\delta = 0.04$.

Evaluation Metrics. We consider the case where $c_\delta \in \{0, 0.04, 0.12\}$. For reference shape normalized to $[-1, 1]$, having a $c_\delta = 0.12$ is very small. We compare the main loss with the addition of PPM-Reg and track the 2-Wasserstein distance up-to the 1-dimensional persistence diagrams along gradient step.

Result. Figure 5 shows the change in PD distance as c_δ increases with the circle Figure 5(a) and union of two circles Figure 5(b). Compared with only using MMD as main loss, adding PPM-Reg consistently converges to a smaller PD distance regardless of the c_δ value. In contrast, when only using MMD, the PD distance increases as c_δ value increases. Figure 5 illustrates the benefit of *explicitly* comparing the difference between topological features with PPM-Reg compared with *implicitly* considering topological features with only MMD when the optimization problem may not converge to near zero.

F UNCONDITIONAL IMAGE GENERATION

F.1 IMPLEMENTATION DETAILS FOR UNCONDITIONAL IMAGE GENERATION

This section fills in the details of the unconditional image generation experiment in Section 6.3.

| λ | $\sigma = 0.05$ | | | $\sigma = 0.5$ | | | $\sigma = 1.0$ | | |
|-----------|-----------------|----------------------|----------------------|----------------|----------------------|----------------------|----------------|----------------------|----------------------|
| | CMMD | FD _{Dinov2} | WD _{latent} | CMMD | FD _{Dinov2} | WD _{latent} | CMMD | FD _{Dinov2} | WD _{latent} |
| 1.0 | 0.74 | 945.27 | 0.6330 | 0.68 | 846.33 | 0.6228 | 0.56 | 780.68 | 0.6080 |
| 5.0 | 0.73 | 928.60 | 0.6310 | 0.72 | 884.40 | 0.6282 | 0.74 | 894.77 | 0.6308 |
| 10.0 | 0.74 | 880.68 | 0.6332 | 0.77 | 922.58 | 0.6379 | 0.71 | 923.50 | 0.6274 |

Table 4: Ablation study on AnimeFace dataset.

| λ | $\sigma = 0.05$ | | | $\sigma = 0.5$ | | | $\sigma = 1.0$ | | |
|-----------|-----------------|----------------------|----------------------|----------------|----------------------|----------------------|----------------|----------------------|----------------------|
| | CMMD | FD _{Dinov2} | WD _{latent} | CMMD | FD _{Dinov2} | WD _{latent} | CMMD | FD _{Dinov2} | WD _{latent} |
| 1.0 | 0.87 | 737.09 | 0.6945 | 0.65 | 704.74 | 0.6744 | 0.81 | 745.39 | 0.6886 |
| 5.0 | 0.72 | 733.66 | 0.6815 | 0.58 | 700.73 | 0.6666 | 0.68 | 695.36 | 0.6768 |
| 10.0 | 0.61 | 690.01 | 0.6691 | 0.69 | 683.35 | 0.6781 | 0.71 | 719.39 | 0.6795 |

Table 5: Ablation study on CelebA dataset.

Implementation Details. The network architectures used in the unconditional image generation in Section 6.3 are shown in Figure 8. As illustrated in Figure 8, g_ω is a ResNet based CNN that takes 128-dimensional noise vector as input. d_θ is a CNN that outputs a 128-dimensional latent vector.

We compare the basic Cramer (Bellemare et al., 2017) value function $\mathcal{V} = \mathcal{L}$, with the use of PPM-Reg $\mathcal{V} = \mathcal{L} + \mathcal{T}$. For the addition of PPM-Reg case, we fix $\lambda_0 = 0.001$, $\lambda_1 = 0.6$, and $s = 1024$. $\lambda = \{1.0, 5.0, 10.0\}$ and $\sigma = \{0.05, 0.1, 0.5\}$ are the tuning parameter. In both cases, the standard Adam optimizer with learning rate 1×10^{-4} is used to train the network. For g_ω , $\beta_1 = 0.0$ and $\beta_2 = 99$. For d_θ , $\beta_1 = 0.5$ and $\beta_2 = 0.99$. The batch size is 192. For the CelebA dataset, the GAN training run for 5440 epochs. For AnimeFace data set, the GAN training run for 7000 epochs.

During training, we compute CMMD for every 160 epochs. We report the CMMD (Jayasumana et al., 2024) and WD_{latent} and FD_{Dinov2} (Stein et al., 2024) with the smallest CMMD value across training epochs. Those quantitative metrics are computed by sampling 10K images from the data set and generating 10k images from the network.

Ablation Study. There are two primary parameters in our topological regularizer. The parameter λ controls the strength of the regularizer, while σ controls the width of the RBF kernel in defining the MMD for PPMs. We provide an ablation study to show how the evaluation metrics change as we vary these parameters in Table 5 for AnimeFace and Table 4 for CelebA.

F.2 FURTHER UNCONDITIONAL IMAGE GENERATION EXPERIMENT

This section introduces supplementary unconditional image generation experiments with an increase in image resolution as well as additional datasets in conjunction with appropriate network architectures.

| | CelebA | | | LSUN Kitchen | | |
|---------------------------------|--------|----------------------|----------------------|--------------|----------------------|----------------------|
| | CMMD | FD_{Dinov2} | WD_{latent} | CMMD | FD_{Dinov2} | WD_{latent} |
| Cramer (Bellemare et al., 2017) | 0.52 | 902.09 | 0.7335 | 1.56 | 1592.06 | 0.7690 |
| Cramer + PPM-Reg | 0.46 | 826.04 | 0.7296 | 1.31 | 1381.22 | 0.7502 |

Table 6: Quantitative evaluation on 64×64 image generation, values are reported at the epoch with the smallest CMMD.

Implementation Details. Similar to Section 6.3, g_ω is a ResNet based CNN that takes 128-dimensional noise vector as input. d_θ is a CNN that outputs a 128-dimensional latent vector. The major difference is instead of just generating 32×32 images as in Section 6.3, we test our PPM-Reg with higher resolution. Specifically, we consider the 64×64 image generation task. To accommodate the increase in modeling complexity, we introduce a new network architecture shown in Figure 9.

To avoid confusion, we will write out our implementation details. We are comparing Cramer (Bellemare et al., 2017) and the addition of PPM-Reg. For the addition of PPM-Reg case, we only fix $\lambda_0 = 0.001$ and $s = 1024$. The value of λ_1 changes as the training epoch runs. Specifically, we adapt cosine annealing (Loshchilov & Hutter, 2016) on λ_1 , the λ_1 value at epoch t term λ_1^t is given by

$$\lambda_1^t = \begin{cases} \lambda_1^{\min} + \frac{1}{2}(\lambda_1^{\max} - \lambda_1^{\min})(1 + \cos(\frac{t}{t_{\text{end}}}\pi)), & \text{if } t \leq t_{\text{end}} \\ \lambda_1^{\min}, & \text{if } t > t_{\text{end}}, \end{cases} \quad (53)$$

where λ_1^{\min} , λ_1^{\max} and t_{end} are user-defined variable. λ_1^{\min} and λ_1^{\max} are the range of the λ_1 , t_{end} is the ending epoch for the cosine annealing. We fix $\lambda_1^{\min} = 0.1$, $\sigma = 0.5$ for both dataset. For CelebA, $\lambda = 1$, $\lambda_1^{\max} = 1$ and $t_{\text{end}} = 1920$. For LSUN Kitchen, $\lambda = 10$, $\lambda_1^{\max} = 0.8$, and $t_{\text{end}} = 260$. The standard Adam optimizer with learning rate 1×10^{-4} is used to train the network. For g_ω , $\beta_1 = 0.0$ and $\beta_2 = 99$. For d_θ , $\beta_1 = 0.5$ and $\beta_2 = 0.99$. The batch size is 192. For the CelebA dataset, the GAN training is run for 2560 epochs, while for the LSUN Kitchen data set, the GAN training is run for 300 epochs.

Dataset and Evaluation Metrics. We add a new dataset LSUN Kitchen (Yu et al., 2015) and also use CelebA (Liu et al., 2015) at a higher resolution. Images are centered and resized to 64×64 .

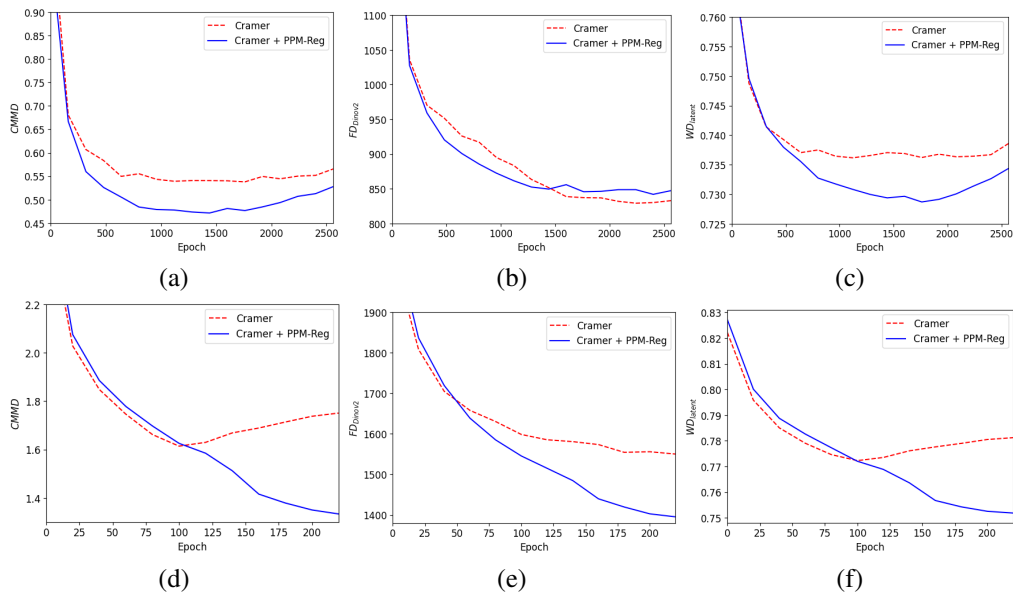


Figure 6: CMMD (a,e), FD_{Dinov2} (b,f) and WD_{latent} (c,g) versus training epochs for the CelebA (a-c) and LSUN Kitchen (d-f) dataset for the 64×64 image generation. 10K samples are randomly generated to compute the distances, and moving averages with a window of 5 are used to smooth the values. For CelebA, distances are recorded every 160 epochs. For LSUN Kitchen, distances are recorded every 20 epochs.

During training, we compute CMMD for every 160 epochs for CelebA and 20 epochs for LSUN Kitchen. We report the CMMD (Jayasumana et al., 2024) and WD_{latent} and FD_{Dinov2} (Stein et al., 2024) with the smallest CMMD value across training epochs. For justification for using the chosen quantitative evaluation metrics, readers can refer to Section 6.3. Those quantitative metrics are computed by sampling 10K images from the data set and generating 10k images from the network.

Result. Figure 6 tracks the three quantitative metrics during training and Table 6 reports the three metrics with the smallest CMMD. While the FD_{Dinov2} metric has comparable values in Figure 6(b), at the point of the smallest CMMD, Cramer + PPM-Reg has a smaller FD_{Dinov2} for CelebA, shown in Table 6. Our quantitative results in Table 6 reinforce the fact that using PPM-Reg improves the generative ability of GANs. Compared to CelebA dataset, using PPM-Reg in the LSUN Kitchen dataset results in a more significant improvement. We conjecture that since LSUN Kitchen is a much larger dataset (2,212,277 training samples) that contains diverse images (i.e. different color tones, layouts), its underlying lower dimensional submanifold has more complex topological features compared with CelebA. The significant improvement gives evidence that PPM-Reg is useful in discovering more complex topological structures in latent space.

G SEMI-SUPERVISED LEARNING

G.1 IMPLEMENTATION DETAILS FOR SEMI-SUPERVISED LEARNING

This section fills in the details of the semi-supervised learning experiment in Section 6.4.

Network Architecture and Implementation Details. The network architectures used in the semi-supervised learning experiment in Section 6.4 are shown in Figure 10. The input noise vector of g_{ω} has dimension of 64. We set the dimension of the output latent vector of d_{θ} as 64.

Specifically, g_{ω} and d_{θ} are trained with the GAN framework for 4,000 epochs using the standard Adam optimizer with learning rate 1×10^{-4} . For g_{ω} , we set $\beta_1 = 0.0$ and $\beta_2 = 99$; for d_{θ} , we set $\beta_1 = 0.5$ and $\beta_2 = 0.99$. The batch size is 192. For Cramer + PPM-Reg, we fix $\lambda_0 = 1$, $\lambda_1 = 90$

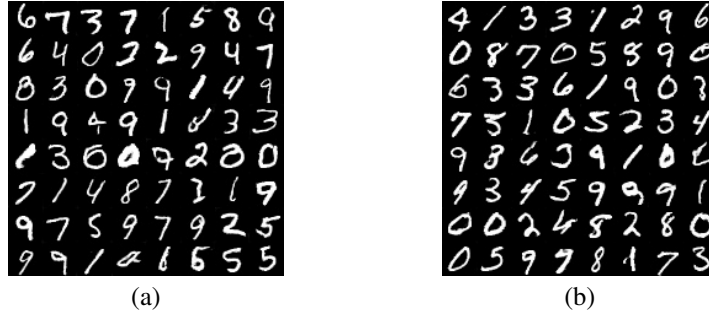


Figure 7: Generated images from SSL experiment from trained g_ω for MNIST using (a) Cramer Distance and (b) PPM-Reg.

and $s = 1024$. $\lambda = \{0.025, 0.05, 0.1\}$ and $\sigma = \{0.05, 0.1, 0.5\}$ are the tuning parameter. After the GAN framework completes the training of g_ω and d_θ , the weights of d_θ are frozen. Using d_θ as feature extraction, the output of d_θ is fed into the classifier. The classifier c_γ is train with the standard Adam optimizer with learning rate 1×10^{-4} where $\beta_1 = 0.1$ and $\beta_2 = 0.99$ for 1000 epochs.

"Baseline" connects d_θ and c_γ and trains as a classifier without first pertaining d_θ with GANs. The standard Adam optimizer with learning rate 1×10^{-4} where $\beta_1 = 0.1$ and $\beta_2 = 0.99$ are use to train the "Baseline" network for 4,000 epochs.

| λ | Fashion-MNIST (200 labels) | | | Fashion-MNIST (400 labels) | | |
|-----------|----------------------------|------------------|------------------|----------------------------|------------------|------------------|
| | $\sigma = 0.05$ | $\sigma = 0.1$ | $\sigma = 0.5$ | $\sigma = 0.05$ | $\sigma = 0.1$ | $\sigma = 0.5$ |
| 0.1 | 75.39 ± 1.12 | 74.96 ± 0.96 | 75.24 ± 1.20 | 75.39 ± 1.12 | 74.96 ± 0.96 | 75.24 ± 1.20 |
| 0.05 | 76.35 ± 1.09 | 76.25 ± 1.30 | 76.81 ± 0.88 | 76.35 ± 1.09 | 76.25 ± 1.30 | 76.81 ± 0.88 |
| 0.025 | 76.42 ± 0.85 | 76.77 ± 1.29 | 76.84 ± 1.23 | 76.42 ± 0.85 | 76.77 ± 1.29 | 76.84 ± 1.23 |

Table 7: Ablation study on Fashion-MNIST dataset with 200/400 labels. Test-set classification accuracy (%) is shown averaged over 10 runs.

| λ | Kuzushiji-MNIST (200 labels) | | | Kuzushiji-MNIST (400 labels) | | |
|-----------|------------------------------|------------------|------------------|------------------------------|------------------|------------------|
| | $\sigma = 0.05$ | $\sigma = 0.1$ | $\sigma = 0.5$ | $\sigma = 0.05$ | $\sigma = 0.1$ | $\sigma = 0.5$ |
| 0.1 | 73.70 ± 2.58 | 70.84 ± 2.56 | 70.16 ± 1.96 | 78.35 ± 1.81 | 76.18 ± 1.87 | 76.67 ± 1.31 |
| 0.05 | 74.35 ± 2.45 | 73.65 ± 1.70 | 73.97 ± 1.24 | 78.99 ± 1.41 | 79.92 ± 1.88 | 78.77 ± 1.48 |
| 0.025 | 74.47 ± 1.65 | 75.78 ± 1.99 | 75.41 ± 2.83 | 79.40 ± 1.65 | 79.33 ± 1.69 | 80.04 ± 1.37 |

Table 8: Ablation study on Kuzushiji-MNIST with 200/400 labels. Test-set classification accuracy (%) is shown averaged over 10 runs.

Ablation Study. We show how the classification accuracy varies with respect to the topological regularization strength λ and the RBF width σ in Table 7 for Fashion-MNIST, Table 8 for Kuzushiji-MNIST, and Table 9 for MNIST.

G.2 FURTHER SEMI-SUPERVISED LEARNING EXPERIMENT

This section introduces supplementary semi-supervised learning experiments with additional datasets in conjunction with appropriate network architectures.

Network Architecture and Implementation Details. Similar to the setup in Section 6.4, g_ω is a deconvolutional network with 64 dimension noise vector as input. d_θ is a CNN with a 64 dimension latent vector as output. The additional SVHM dataset is more intricate than the MNIST variants evaluated in Section 6.4, as it is a color image dataset with higher resolution. To tackle the increase in

| λ | MNIST (200 labels) | | | MNIST (400 labels) | | |
|-----------|--------------------|------------------|------------------|--------------------|------------------|------------------|
| | $\sigma = 0.05$ | $\sigma = 0.1$ | $\sigma = 0.5$ | $\sigma = 0.05$ | $\sigma = 0.1$ | $\sigma = 0.5$ |
| 0.1 | 96.34 \pm 0.29 | 96.32 \pm 0.20 | 96.18 \pm 0.19 | 97.19 \pm 0.28 | 97.06 \pm 0.28 | 97.07 \pm 0.26 |
| 0.05 | 96.61 \pm 0.37 | 96.62 \pm 0.39 | 96.22 \pm 0.59 | 97.29 \pm 0.20 | 97.33 \pm 0.21 | 97.16 \pm 0.25 |
| 0.025 | 96.13 \pm 0.42 | 95.97 \pm 0.37 | 95.91 \pm 0.55 | 97.04 \pm 0.27 | 96.92 \pm 0.20 | 97.2 \pm 0.25 |

Table 9: Ablation study on MNIST with 200/400 labels. Test-set classification accuracy (%) is shown averaged over 10 runs.

input dimension and the complexity of modeling the dataset, we introduce a new network architecture shown in Figure 11.

The training setup largely follows the previous experiment; the major difference is the number of training epochs. Specifically, g_ω and d_θ are trained with the GAN framework for 1,200 epochs. The standard Adam optimizer with learning rate 1×10^{-4} is used to train the network. For g_ω , $\beta_1 = 0.0$ and $\beta_2 = 99$. For d_θ , $\beta_1 = 0.5$ and $\beta_2 = 0.99$. The batch size is 192. For Cramer + PPM-Reg, we fix $\lambda_0 = 1$, $\lambda_1 = 90$ and $s = 1024$. $\lambda = \{0.025, 0.05, 0.1\}$ and $\sigma = \{0.05, 0.1, 0.5\}$ are the tuning parameter. After the GAN framework completes the training of g_ω and d_θ , the weights of d_θ are frozen. Using d_θ as feature extraction, the output of d_θ is fed into the classifier. The classifier c_γ is trained with the standard Adam optimizer with learning rate 1×10^{-4} where $\beta_1 = 0.1$ and $\beta_2 = 0.99$ for 1000 epochs. The standard Adam optimizer with learning rate 1×10^{-4} where $\beta_1 = 0.1$ and $\beta_2 = 0.99$ are use to train the "Baseline" network for 4,000 epochs.

Dataset and Evaluation Metrics. We compare the SSL performance with the dataset SVHN. In this experiment, 400 and 600 labels are randomly sampled from the data set. Because of the random nature involved in selecting a few labels, we conducted the experiments ten times and provided the statistics of the highest test-set accuracy achieved.

| Number of labels | SVHN | |
|------------------|------------------------------------|------------------------------------|
| | 400 | 600 |
| Baseline | 44.68 \pm 2.44 | 53.68 \pm 4.15 |
| Cramer | 38.12 \pm 1.75 | 43.23 \pm 1.14 |
| Cramer + PPM-Reg | 57.20 \pm 1.51 | 61.39 \pm 0.66 |

Table 10: Test-set classification accuracy (%) on SVHN with 400 and 600 labeled examples. The average and the error bar are computed over 10 runs.

| λ | SVHN (400 labels) | | | SVHN (600 labels) | | |
|-----------|-------------------|------------------|------------------|-------------------|------------------|------------------|
| | $\sigma = 0.05$ | $\sigma = 0.1$ | $\sigma = 0.5$ | $\sigma = 0.05$ | $\sigma = 0.1$ | $\sigma = 0.5$ |
| 0.1 | 55.66 \pm 1.78 | 57.20 \pm 1.51 | 54.84 \pm 1.21 | 59.48 \pm 1.26 | 61.39 \pm 0.66 | 59.13 \pm 0.95 |
| 0.05 | 47.56 \pm 1.67 | 56.24 \pm 1.25 | 52.41 \pm 1.49 | 50.73 \pm 1.06 | 60.08 \pm 0.84 | 60.91 \pm 1.19 |
| 0.025 | 55.96 \pm 1.03 | 56.96 \pm 1.92 | 55.35 \pm 1.06 | 59.13 \pm 0.95 | 56.45 \pm 1.41 | 58.97 \pm 1.00 |

Table 11: Ablation study on SVHN with 400/600 labels. Test-set classification accuracy (%) is shown averaged over 10 runs.

Result. Table 10 shows the test classification accuracy. An ablation study is provided in Table 11. SVHN contains 72,657 training samples and 400 and 600 labels constitute only 0.55% and 0.82% of the original datasets, respectively. The results follow the same characteristic in Section 6.4, only using Cramer does not improve the classification accuracy in SSL. In contrast, the use of PPM-Reg results in a notable improvement in classification accuracy. Specifically, using PPM-Reg with 400 labels yields a 12.52% increase in accuracy compared to the Baseline. The consistent outcome with more complex datasets and network architecture reinforces our claim that PPM-Reg can help learn a more informative latent encoding thereby improving SSL performance.

H NETWORK ARCHITECTURE

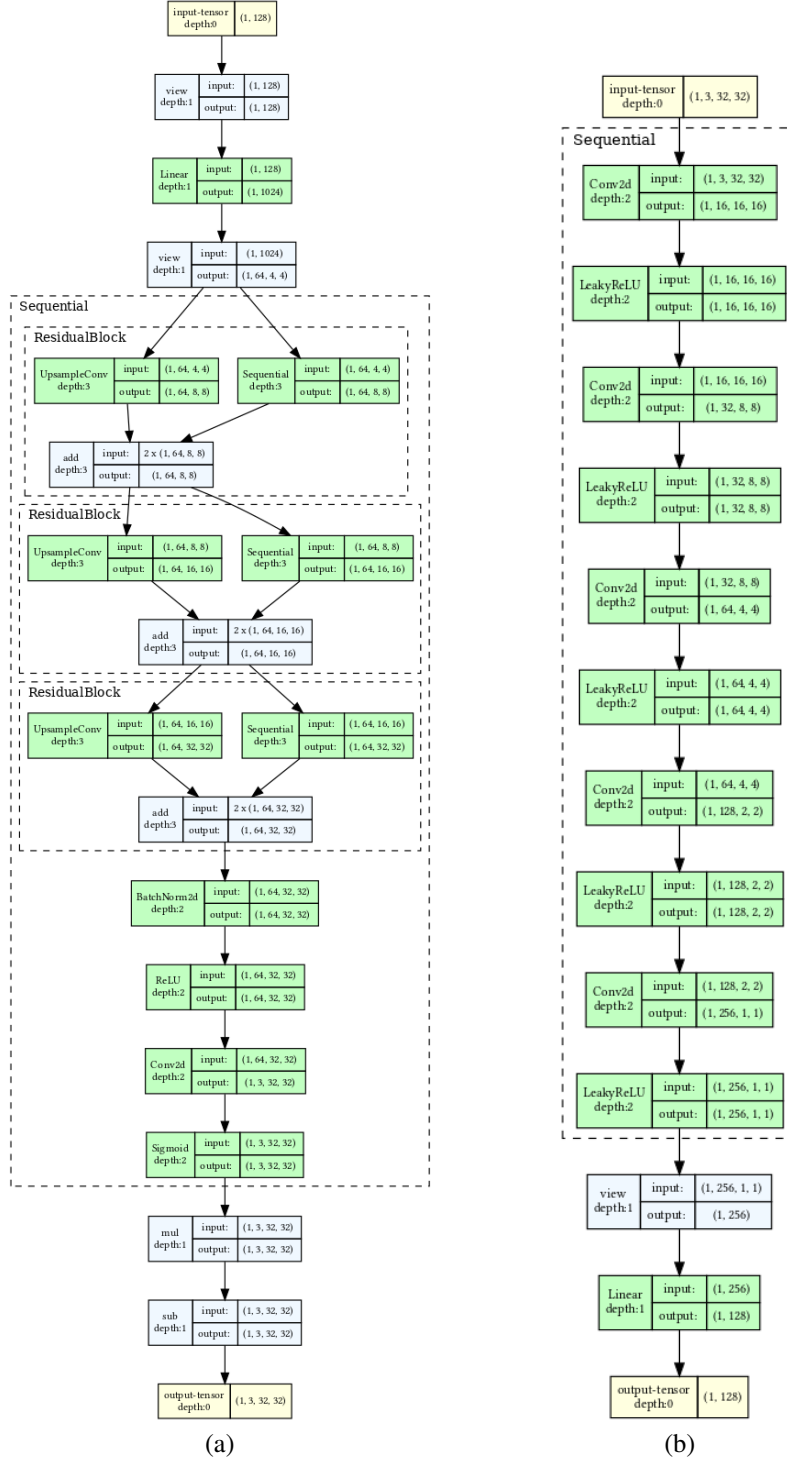


Figure 8: Network architecture of generator (a), discriminator (b) for 32×32 unconditional image generation.

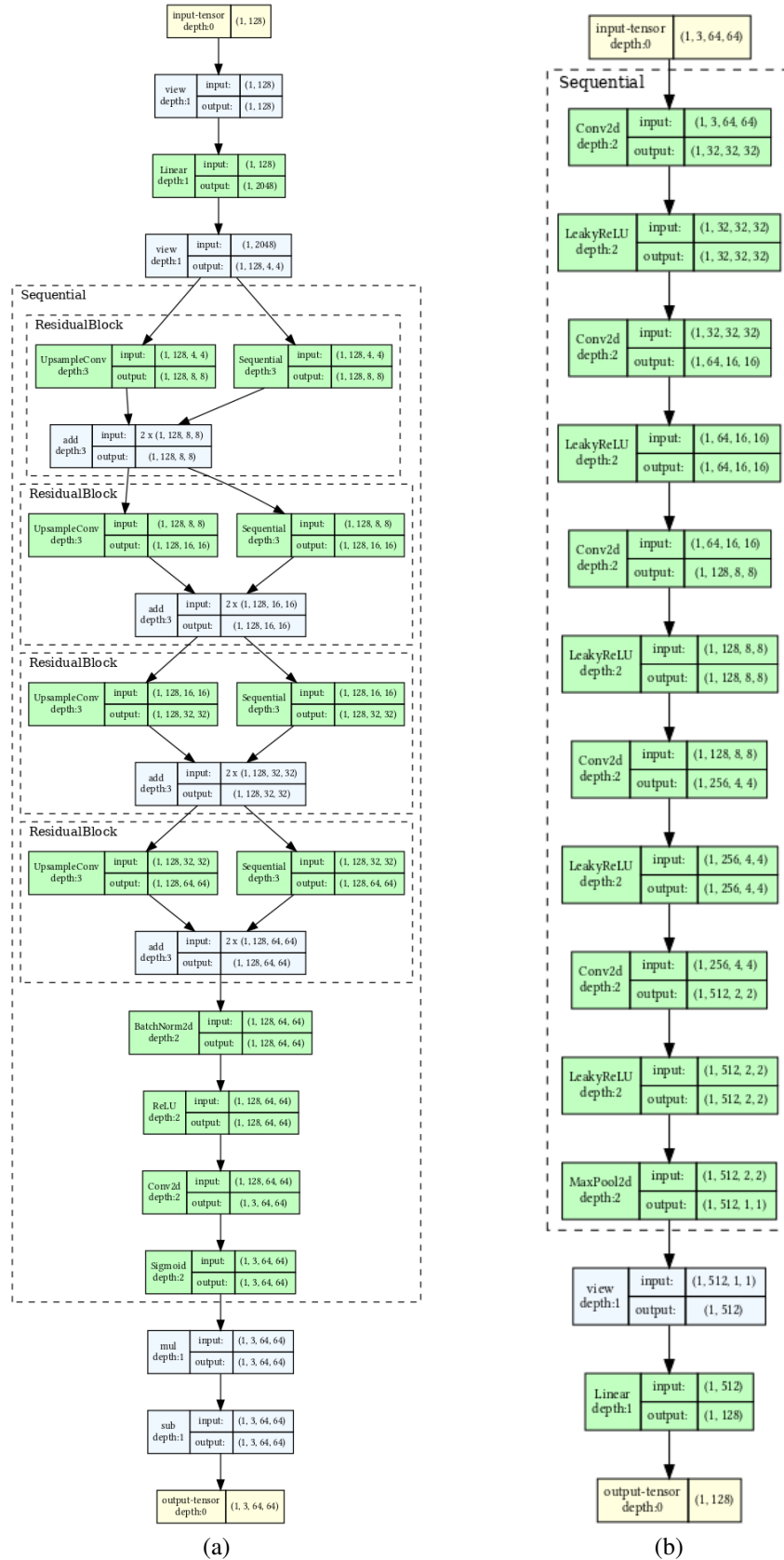


Figure 9: Network architecture of generator (a), discriminator (b) for 64×64 unconditional image generation.

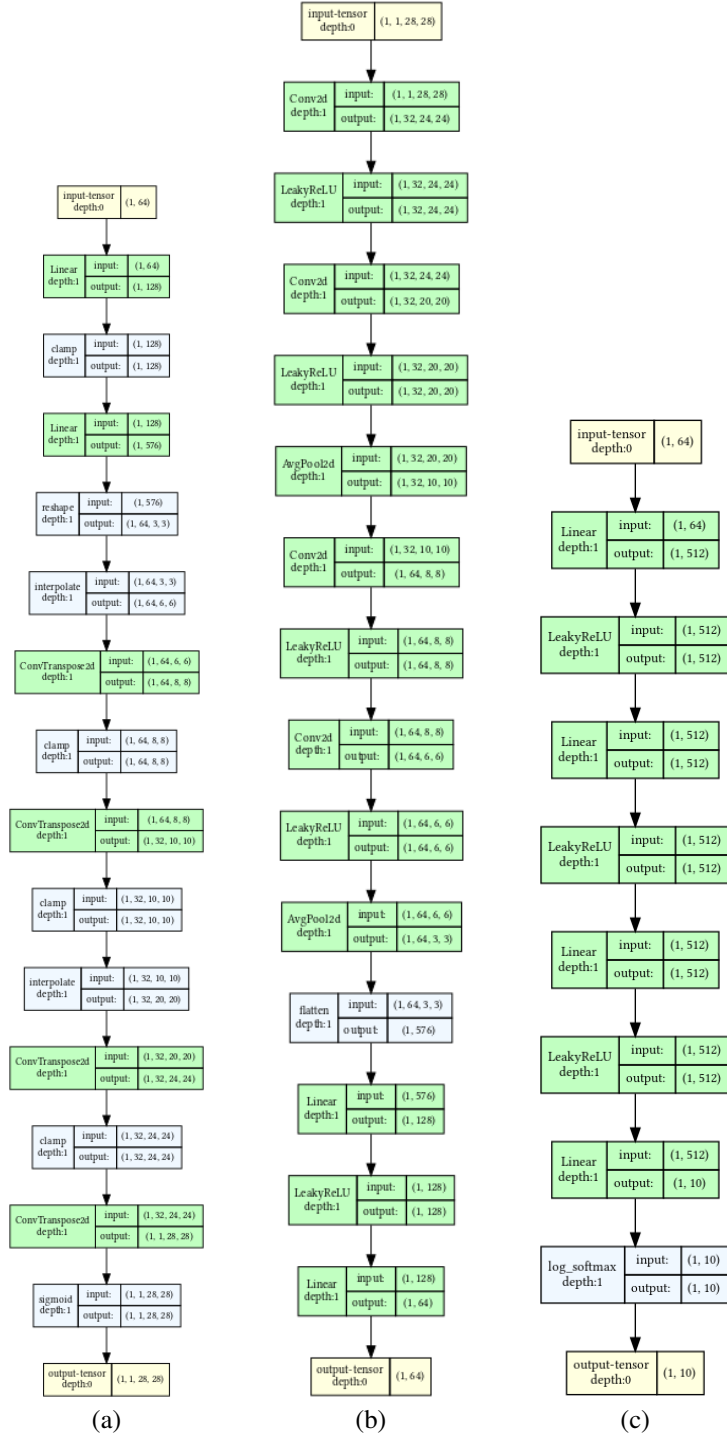


Figure 10: Network architecture of generator (a), discriminator (b) and classifier (c) for semi-supervised learning for MNIST variants.

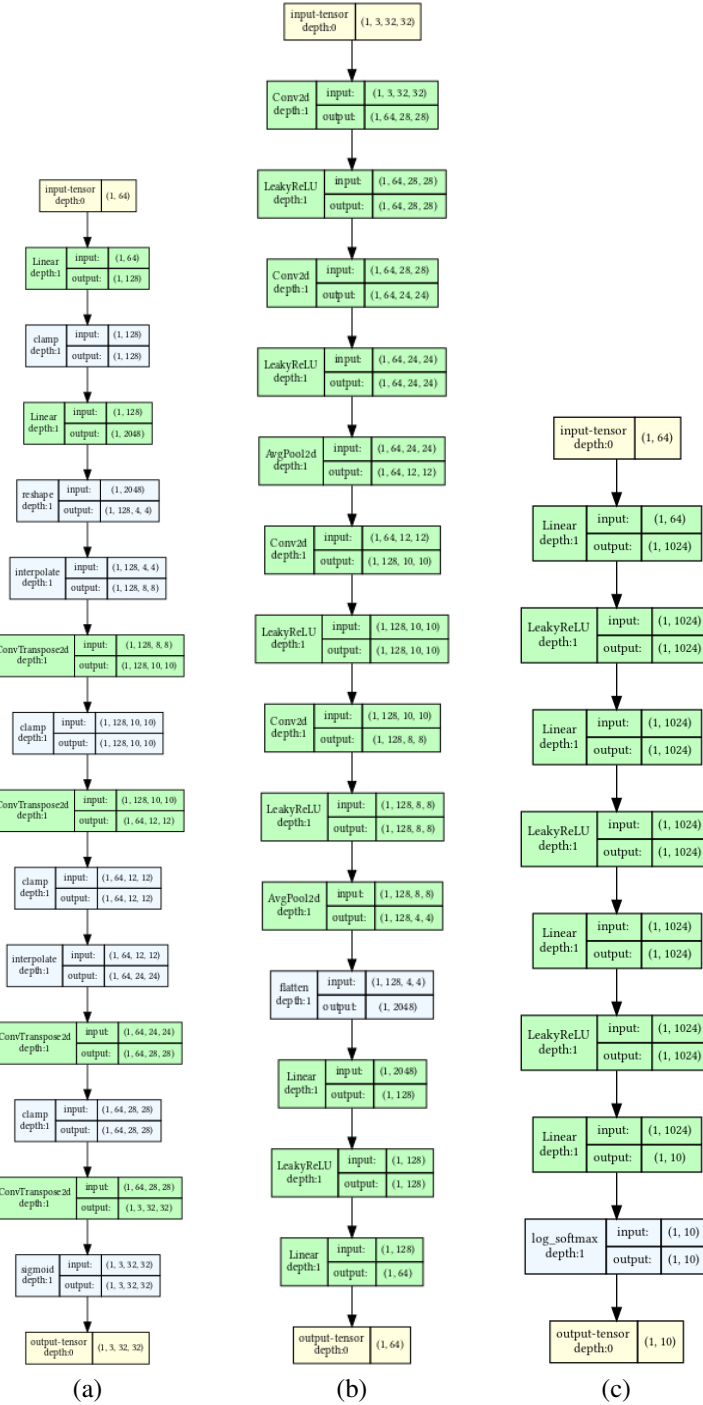


Figure 11: Network architecture of generator (a), discriminator (b) and classifier (c) for semi-supervised learning for SVHN dataset.